

Towards  Quantum Computation with  
Ultracold Fermi Atoms

Yanay Florshaim






This work was performed under the supervision of Prof. Yoav Sagi


## Abstract

In quantum mechanics, the dimension of the Hilbert space grows exponentially with the system size. Therefore, a classical calculation of many-body quantum states becomes practically impossible for already a small number of particles. Richard Feynman was the first to suggest a different paradigm to overcome this difficulty - a quantum computational machine ("Quantum Computer"). The quest to build a quantum computer has been going on for more than 20 years, but so far, single experimental platforms have emerged as technologically superior. I will present our suggestion for a new platform based on ultracold  $^{40}\text{K}$  fermionic atoms held in an optical microtrap. In our scheme, quantum information can be stored in the internal states of these atoms or in vibrational states of the trap. Single qubit gates are implemented by coupling the atom to an external field, and a universal two-qubit  $\sqrt{\text{SWAP}}$  gate is implemented by a novel protocol that takes advantage of our ability to precisely control the tunnelling energy and the interaction energy between two atoms at two adjacent traps. I will present numerical simulations of the qubits and gates and report on our progress in the lab towards testing our ideas in real life.


## Acknowledgments

 First I would like to thank my supervisor, Prof. Yoav Sagi, for his great support in every aspect of my M.Sc. Yoav's contagious enthusiasm for research and his vast knowledge are all a student can hope for from a supervisor. To work in a new lab is not an easy task, with many difficulties and mistakes along the way, but due to Yoav's optimistic vision and willingness to teach and share his wisdom, things always turned out for the best.



I would like to thank Dr.  Andrey Gandman, our research associate, for his help in experimental issues. In addition, I would like to thank Dr. Jonathan Nemirovsky for his theoretical work including  numerical simulations and calculations.

I would like to thank all my current lab colleagues:  stya Sekadorov, Iris Eitan and Gal Ness, since much of work was done in collaboration with them, I want to thank them for the professional help and good advice.

I would like to thank my parents for their support and encouragement during my studies.

Finally, I want to thank my wife Sara and my daughters Arbel, Be'er  and Yahav for their love, support, and assistance during my studies.

# Contents

<b>1</b>	<b>Introduction</b>	<b>1</b>
<b>2</b>	<b>New platform of quantum computation</b>	<b>6</b>
2.1	The new scheme . . . . .	6
2.1.1	The Qubit . . . . .	6
2.1.2	Preparation of the Initial State . . . . .	7
2.1.3	Quantum gates . . . . .	8
2.1.4	Ability to Measure the Results . . . . .	19
2.1.5	Scalability . . . . .	20
2.2	Theoretical simulation and calculation . . . . .	21
<b>3</b>	 <b>ultra-cold atoms</b>	<b>27</b>
3.1	laser cooling technique . . . . .	27
3.1.1	Doppler cooling . . . . .	27
3.1.2	Sisyphus Cooling . . . . .	28
3.1.3	Gray Molasses Cooling . . . . .	28
3.1.4	Magneto optical trap  . . . . .	29
3.1.5	Magnetic field for MOT . . . . .	30
3.2	Raman Sideband cooling . . . . .	32
3.3	Magnetic trap - QUIC configuration . . . . .	32
3.4	Optical trap . . . . .	34
<b>4</b>	<b>The experimental machines</b>	<b>36</b>
4.1	The experimental systems . . . . .	36
4.2	MOT . . . . .	39
4.2.1	Coils setup . . . . .	39
4.2.2	Lasers setup . . . . .	40
4.2.3	Saturated Absorption Spectroscopy (SAS) . . . . .	43

4.2.4	Offset locking . . . . .	46
4.2.5	Measurements of the number of atoms . . . . .	46
4.2.6	Temperature Measurement with Release & Recapture Technique . . . . .	49
4.3	$D_1$ cooling . . . . .	51
4.3.1	Lasers setup . . . . .	51
4.3.2	High Frequency Electro-Optic-Modulator . . . . .	52
4.3.3	Measurement of the $D_1$ Frequency Resonance . . . . .	57
4.3.4	Temperature and atoms number measurement by Time Of Flight (TOF ) technique	57
4.4	Optical Trap . . . . .	59
4.4.1	Microtrap waist measurement . . . . .	60
4.4.2	Measurement of a microtrap waist with an optical chopper . . . . .	61
4.4.3	Measurement of the microtrap waist with a piezoelectric actuator and Michelson interferometer . . . . .	61



**5 Summery and Future Plan**

# 1 Introduction

In quantum mechanics, the dimension of the Hilbert space grows exponentially with system size. To represent a quantum state with  $n$  particles in classical computation, we need an order of  $C^n$  bits, where  $C$  is a constant. Therefore, the possibility of calculating many-body quantum states in classical computing becomes practically impossible. To overcome this problem, it was first proposed by Feynman to use a quantum computational machine (Quantum Computer) [1]. A quantum computer is able to not only simulate quantum dynamics, but also solve complex mathematical problems. In addition, the quantum computer is much faster than classical computers in solving factorial problems [2] and in database searching [3]. For two decades, researchers have been trying to implement quantum computation using different platforms, but all these platforms suffer from inherent experimental limits [4, 5, 6, 7, 8, 9]. Here, we present a new platform of a quantum computer system with ultracold fermionic atoms. We take advantage of the fermionic statistics and ultracold atom system benefits (Feshbach resonance and the ability to capture single atoms in optical traps) to perform a new protocol for quantum gate operators.

Quantum computer system requirements, as stated by DiVincenzo [10], should comply with five conditions:

- **Quantum state.** The quantum state encapsulates the quantum information in a quantum computer. The state is usually spanned by two basis vectors,  $|0\rangle$  and  $|1\rangle$ , and the qubit state is defined by

$$|\psi\rangle = \alpha |0\rangle + \beta |1\rangle$$

where  $\alpha$  and  $\beta$  are complex numbers. When the qubit is measured, with the probability of  $|\alpha|^2$  it is in a state  $|0\rangle$  and with a probability of  $|\beta|^2$  in a state  $|1\rangle$ , satisfying the following relation:

$$|\alpha|^2 + |\beta|^2 = 1$$

since the probabilities must sum to one.

- **Preparation of the Initial State.** The initial state of the qubit should be capable of being prepared. The particular initial state is of little importance, as we can transform it to any other state using several quantum gates. However, it is important that the initial state can be created with high fidelity.
- **Quantum gates.** To perform any quantum calculation, we need several unitary operations ("Quantum Gates") that form a universal set, namely, any other operation can be decomposed to a series of gate operations taken from this set. The quantum gates operate on one or two qubits. Examples of one-qubit gates include the Hadamard gate, the phase gate, and the  $\pi/8$  gate. The two-qubit gate is a C-NOT gate. In place of a C-NOT gate, it is also possible to use a  $\sqrt{\text{SWAP}}$  gate [11].

1. **Hadamard gate.** The Hadamard gate is a one-qubit rotation. This gate maps the qubit states  $|0\rangle$  and  $|1\rangle$  to two superpositions with equal weight.

$$U = \frac{|0\rangle + |1\rangle}{\sqrt{2}} \langle 0| + \frac{|0\rangle - |1\rangle}{\sqrt{2}} \langle 1|$$

or in a matrix representation

$$U = \frac{1}{\sqrt{2}} \begin{bmatrix} 1 & 1 \\ 1 & -1 \end{bmatrix}$$

In addition, Hadamard gate is essentially a "beam splitter" for the two "modes"  $|0\rangle$  and  $|1\rangle$ , namely  $|0\rangle \rightarrow \frac{|0\rangle + |1\rangle}{\sqrt{2}}$  and  $|1\rangle \rightarrow \frac{|0\rangle - |1\rangle}{\sqrt{2}}$ .

2. **Phase gate.** Phase gate is a one-qubit gate that leaves the basis  $|0\rangle$  without a change while transforming  $|1\rangle \rightarrow e^{i\phi} |1\rangle$ .

$$U = |0\rangle \langle 0| + e^{i\phi} |1\rangle \langle 1|$$

or in a matrix representation

$$U_\phi = \begin{bmatrix} 1 & 0 \\ 0 & e^{i\phi} \end{bmatrix}$$

Where  $\phi$  is the *phase shift*. Some common examples are the phase gate with  $\phi = \pi/2$ , the  $\pi/8$  gate with  $\phi = \pi/4$  and the Pauli-Z gate with  $\phi = \pi$ .

3.  **$\sqrt{\text{SWAP}}$  gate.** A  $\sqrt{\text{SWAP}}$  gate is operated on the mixed states and swapped with them half way, namely,  $|1, 0\rangle \rightarrow \frac{1}{2} [(1+i)|1, 0\rangle + (1-i)|0, 1\rangle]$  and  $|0, 1\rangle \rightarrow \frac{1}{2} [(1-i)|1, 0\rangle + (1+i)|0, 1\rangle]$ . In a matrix representation, the gate is defined by

$$U_{\sqrt{\text{swap}}} = \begin{bmatrix} 1 & 0 & 0 & 0 \\ 0 & \frac{1}{2}(1+i) & \frac{1}{2}(1-i) & 0 \\ 0 & \frac{1}{2}(1-i) & \frac{1}{2}(1+i) & 0 \\ 0 & 0 & 0 & 1 \end{bmatrix} \quad (1)$$

with respect to the basis  $|00\rangle, |01\rangle, |10\rangle, |11\rangle$ .

By using all these gates we can reduce any unitary operation of  $n$  qubits to a cumulative series of these gates [12].

- **Ability to Measure the Result.** The ability to measure the final state of the system is required for all computation schemes.
- **Scalability.** All physical resources (such as space, money and number of components) should not scale as  $X^n$ , where  $X$  is some constant, and  $n$  is the number of qubits. This requirement ensures that the system is technically feasible.

In quantum the phase between states are determinate and the system is coherent. However, in the real world, a quantum computer is not completely isolated and suffers from gate fidelity being less than one. Therefore, the coherence time decay of the state with time  $T_D$  (decoherence time). The time  $T_D$  is also indicated by the results of the quantum-error correction algorithm that can find and correct the same errors in the quantum state [10, 13]. To implement error correction, we demaned




that the decoherence time is much longer than the gate operation timescale  $T_{gate}$  times the typical number of operation  $N$ .


$$\frac{N \cdot T_{gate}}{T_D} \ll 1 \quad (2)$$




To date, attempts have been made to use different physical systems to meet these requirements and realize a quantum computer. For example, in an optical system, the polarization of a photon is taken as a state and optical component, such as polarizing beam splitters, and wavelength plates are used to manipulate the state. Optical systems suffer from photons not interacting; therefore, it is quite difficult to implement two qubit gates [6]. Another platform of quantum calculations is ion traps [4, 5]. Ion traps use the internal state of the ion as the qubit, and quantum gates are implemented using the coupling of the ions to lasers. These systems are probably the closest to a successful implementation, but there are unsolved issues remain with the scalability and heating from the electrodes. Another platform that has been investigated is based on localized electron spins as qubits in quantum dots [8]. The interaction between the spins can realize the quantum gates. The interaction and the detection are performed using lasers. The main problem in this platform is the strong coupling of the qubit to a noisy bath (i.e., phonons), which this limits the ratio of operation time ( $\sim 10$  psec) to decoherence gate-operation time ( $\sim 1$  nsec). Another platform that could theoretically serve to perform quantum computation is neutral atoms in a 1-Dimensional (1D) optical lattice [7]. In this method, they used two sub-level ( $m_f$ ) in the ground state of an optical lattice and described a one qubit-gate with Raman sideband transition ( $t_{\pi/2} \sim 150$  nsec) and with RF pulse ( $t_{\pi/2} \sim 30$   $\mu$ sec). In addition, they use a movable optical tweezer for the two-qubits gate to transport qubit to another one.

In this thesis, we present a new platform of quantum computation that is based on fermionic atoms in an optical microtrap. The basis for this platform is the fermionic statistic of the qubits. In addition, with ultracold atoms, we can control the interaction between atoms by using Feshbach resonance. Furthermore, the depth of the micro-trap, shape, and position can be controlled dynamically.

In recent years, there has been substantial experimental progress with preparation and measurement of individual atoms in the ground state of an optical microtrap [14, 15]. Several techniques have been used to accomplish this:

1. Light-Assisted Collisions (LAC) can reduce the number of atoms by shining the atoms with a near resonant laser. By carefully tuning the frequency, it is possible to increase the probability that one of the atoms will leave the trap while the other will stay.  As one by one by intensifying their interaction [16]. After the LAC has been used to remove all atoms other than one, it is possible to use the Raman side-band cooling technique to cool this single atom to the ground state of the trap [17].
2. By loading spin polarized atoms to a microtrap with one state or several atoms to a low optical microtrap (with several states) and then creating a linear potential that removes all bound states other than one, it is possible to end with only a single atom in one state[18].

The measurement of a single fermion  $^{40}\text{K}$  atom in a trap is clearly not a simple task. In this field,  there are few studies that have succeeded in doing so [14, 15, 17]. In these studies, a sideband cooling technique was employed to cool the atoms while measuring the fluorescence.

Our platform is based on ultracold fermion ( $^{40}\text{K}$ ) neutral atoms trapped in an optical micro-trap. There still remain some questions regarding the experimental system that are discussed in next chapters.  Chapter 2, presents the theory behind our proposed scheme.  Chapter 3 gives some relevant ultracold-atoms background. Chapter 4  presents the experimental work performed in route to implementing the new computation scheme.

## 2 New platform of quantum computation

This chapter explains how we fulfill the five principles mentioned in the introduction. The  $\sqrt{SWAP}$  gate was developed by Dr. Jonathan Nemirovsky, and the numerical simulations were performed with a code that was also developed by Dr. Nemirovsky.

### 2.1 The new scheme

Our new platform is based on neutral ultracold  $^{40}\text{K}$  atoms. This chapter describes the five conditions for quantum computation (1) and how they are realized in our method.

#### 2.1.1 The Qubit

Our quantum computer is based on two internal energy levels of a single atom in a microtrap. We choose  $|0\rangle = |9/2, -9/2\rangle$  and  $|1\rangle = |9/2, -7/2\rangle$  with notation  $|f, m_f\rangle$ , where  $f$  is the total atomic spin, and  $m_f$  is the projection in  $z$  direction (set by external magnetic field). We can choose any two  $m_f$  states, but we want to control the interaction between the atoms by means of a Feshbach resonance [19]. The Feshbach resonance between  $m_f = -9/2$  and  $m_f = -7/2$  is at  $B = 202.2$  G [20]. We can also work in spin states  $|0\rangle = |9/2, -9/2\rangle$  and  $|1\rangle = |9/2, -5/2\rangle$  or  $|0\rangle = |9/2, -7/2\rangle$  and  $|1\rangle = |9/2, -5/2\rangle$ . Their Feshbach resonance is  $B_{-\frac{9}{2}, -\frac{5}{2}} = 224.21$  G and  $B_{-\frac{7}{2}, -\frac{5}{2}} = 174$  G [20]. However, with these states, there is a possibility of spin-exchange collisions, which means that the qubit can leave the designated Hilbert space. The states  $|9/2, -9/2\rangle$  and  $|9/2, -7/2\rangle$  are sensitive to magnetic field fluctuation which will lead to shortening the coherence time. Therefore, when a qubit is not needed for a gate operation we would like to store it in insensitive states. One option to do it is to transfer  $|9/2, -7/2\rangle_{n=0} \rightarrow |9/2, -9/2\rangle_{n=1}$  using Raman transition 3.2. Then the qubit has two energy states but they have the same  $m_f$  and hence have the same magnetic dipole moment. Another possibility is to find two states that have the same sensitivity to a magnetic field (like in an atomic clock [21]). In  $^{40}\text{K}$ , we can use the states  $|9/2, 7/2\rangle_{n=0}$  and  $|7/2, 7/2\rangle_{n=0}$  which are insensitive to a magnetic field at  $B \approx 357$  G (figure 1). The transformation can be done by first flipping the  $m_f$  from negative to positive ( $|9/2, -9/2\rangle_{n=0} \rightarrow |9/2, 9/2\rangle_{n=0}$  and  $|9/2, -7/2\rangle_{n=0} \rightarrow |9/2, 7/2\rangle_{n=0}$ ). It can be done by an adiabatic rapid passage gate that is induced by an RF field that is frequency swept across all the magnetic sublevels [22].

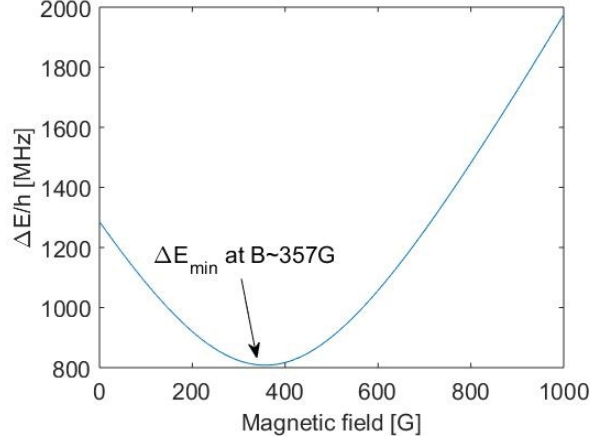


Figure 1: The energy difference between the state  $|9/2, 7/2\rangle_{n=0}$  and  $|9/2, 7/2\rangle_{n=1}$  of the  $^2S_1$  ground state in  $^{40}K$  vs. external magnetic field. The minimum of the first derivative is insensitive to magnetic field (in first order). Using these states we can minimize the decoherence time due to fluctuation in external magnetic field.

Then, with a microwave transition or Raman transition, we can transfer  $|9/2, 9/2\rangle_{n=0} \rightarrow |7/2, 7/2\rangle_{n=0}$ .

### 2.1.2 Preparation of the Initial State

In our method, the initial state requires a single atom state in each qubit. As mentioned in [15], the preparation of one atom in a microtrap can be performed in two ways.

The first method (Fast approach) is based on loading several atoms ( $\sim 10$ ) from a 3-Dimensional (3D) Magneto-Optical-Trap directly to an optical microtrap and with a LAC [16] with a blue detuning laser from the  $D_1$  transition, reducing the atom's number to one (this study has been performed with bosonic  $^{85}Rb$ ). When the trap contains a single atom, we can cool the atom to the ground state with Raman sideband cooling [17]. This process grants two more features. We can measure the fluorescence and calculate the atom number at the optical microtrap (zero, one, or more). Additionally, we can know which qubit is empty and not use it for the quantum calculation.

The second way (Degenerate fermi gas) is to reduce the trap depth until there is only a single bound state left [18]. In [18] it was shown that by using a magnetic field with a gradient the number of atoms up to single atom trapped ( $^6Li$ ) can be controlled. To obtain high occupation probability of the

lowest state due to Fermi-Dirac statistics, such an experiment must begin at very low temperatures  $T/T_f < 0.5$ , in other words,  $T \sim 40$  nK. The time it takes to prepare atoms at this temperature is about 80 seconds.

In Table 1, I compare these two systems. The advantages of the fast approach are rapid data acquisition, and it is experimentally simpler, but here may be a higher final temperature of the captured atom. Also, there are many unknowns with this method that still need to be investigated before we can conclude that this approach is viable. The advantages of the degenerate fermi gas is low final temperature of the trapped atom, but the disadvantage is long preparation time ( $\sim 80$  sec). Chapter 4 presents the two systems in more detail.

	Fast approach	Degenerate fermi gas
Number of Vacuum 1	One or Two	Two or Three
2D and 3D MOT (15 sec)	maybe just 3D	✓
$D_1$ cooling (20 msec)	✓	✓
Magnetic Trap & RF Evaporation (1 sec)	X	✓
Optic or Magnetic Transfer (1-2 sec)	X	✓
Optic Evaporation	X	✓
Sideband Cooling ( $\sim 2$ sec)	✓	X

Table 1: A comparison between the two systems. The table shows that the preferable system in terms of time is the one using light-assisted collisions. However, we are unsure if these will succeed.

### 2.1.3 Quantum gates

After preparing one or two qubits made of single atoms, we need to be able to perform quantum-gate operation. To call our system a Quantum Computer, as was explained in [1], we need to adapt the **Hadamard gate**, the **phase gate**,  **$\pi/8$  gate**, and the  **$\sqrt{\text{SWAP}}$  gate** to our system.

**Single qubit gates.** An arbitrary single qubit state can be written

$$|\psi\rangle = e^{i\gamma} \left( \cos \frac{\theta}{2} |0\rangle + e^{i\phi} \sin \frac{\theta}{2} |1\rangle \right)$$

where  $\theta$ ,  $\phi$ , and  $\gamma$  are real numbers. The numbers  $0 \leq \theta \leq \pi$  and  $0 \leq \phi \leq 2\pi$  define a point on a unit three-dimensional sphere, which is commonly called the *Bloch sphere*. A qubit state with an arbitrary

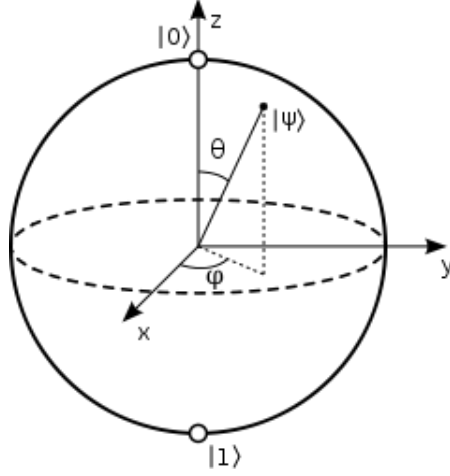


Figure 2: *Bloch sphere*

value of  $\gamma$  is represented by a point on the Bloch sphere, as the factor of  $e^{i\gamma}$  has no observable effects.

We can then write the following:

$$|\psi\rangle = \cos \frac{\theta}{2} |0\rangle + e^{i\phi} \sin \frac{\theta}{2} |1\rangle$$

The Bloch sphere is  $S^2$ , which can be embedded in  $\mathbb{R}^3$  using the following map

$$f : (r = 1, \phi, \theta) \rightarrow (\cos \phi \sin \theta, \sin \phi \sin \theta, \cos \theta)$$

The rotations of Bloch vectors can be generated by Pauli matrices  $\hat{\sigma}_x = \begin{pmatrix} 0 & 1 \\ 1 & 0 \end{pmatrix}$ ,  $\hat{\sigma}_y = \begin{pmatrix} 0 & -i \\ i & 0 \end{pmatrix}$

and  $\hat{\sigma}_z = \begin{pmatrix} 1 & 0 \\ 0 & -1 \end{pmatrix}$ . Therefore, the rotation around the axes is given by

$$R_x(\theta) \equiv e^{-i\frac{\theta}{2}\hat{\sigma}_x} = \cos\frac{\theta}{2}\hat{\mathbb{1}} - i\sin\frac{\theta}{2}\hat{\sigma}_x = \begin{bmatrix} \cos\frac{\theta}{2} & -i\sin\frac{\theta}{2} \\ -i\sin\frac{\theta}{2} & \cos\frac{\theta}{2} \end{bmatrix}$$

$$R_y(\theta) \equiv e^{-i\frac{\theta}{2}\hat{\sigma}_y} = \cos\frac{\theta}{2}\hat{\mathbb{1}} - i\sin\frac{\theta}{2}\hat{\sigma}_y = \begin{bmatrix} \cos\frac{\theta}{2} & -\sin\frac{\theta}{2} \\ \sin\frac{\theta}{2} & \cos\frac{\theta}{2} \end{bmatrix}$$

$$R_z(\theta) \equiv e^{-i\frac{\theta}{2}\hat{\sigma}_z} = \cos\frac{\theta}{2}\hat{\mathbb{1}} - i\sin\frac{\theta}{2}\hat{\sigma}_z = \begin{bmatrix} \exp(-i\frac{\theta}{2}) & 0 \\ 0 & \exp(i\frac{\theta}{2}) \end{bmatrix}$$

Any unitary transformation on a single qubit can be decomposed into a rotation in the Bloch sphere around some axis  $\hat{n}$  by an angle  $\theta$  multiplied by a global phase  $\phi$

$$U = e^{i\phi} R_{\hat{n}}(\theta)$$

Next, we define the single-qubit gates using these terms.

- **Hadamard gate.** A Hadamard gate operator can be represented by rotations around the  $\hat{x}$  and  $\hat{z}$  axes. We choose  $\theta = \pi/2$ ,  $\phi = \pi/2$ , and  $\hat{n} = (1, 0, 1)/\sqrt{2}$

$$\begin{aligned} U_{\text{hadamard}} &= e^{i\frac{\pi}{2}} R_{\hat{n}}(\pi) \\ &= i \left[ \cos\frac{\pi}{2}\hat{\mathbb{1}} - i\sin\frac{\pi}{2} \left( \frac{\hat{\sigma}_x + \hat{\sigma}_z}{\sqrt{2}} \right) \right] \\ &= \frac{1}{\sqrt{2}} \begin{bmatrix} 1 & 1 \\ 1 & -1 \end{bmatrix} \end{aligned}$$

- **Phase gate.** A Phase Gate Operator can be represented by taking  $\theta = \pi/2$ ,  $\phi = \pi/4$ , and

$$\hat{n} = (0, 0, 1)$$

$$U_{\pi/2} = e^{i\frac{\pi}{4}} R_z\left(\frac{\pi}{2}\right) = e^{i\frac{\pi}{4}} \begin{bmatrix} \exp(-i\frac{\pi}{4}) & 0 \\ 0 & \exp(i\frac{\pi}{4}) \end{bmatrix} = \begin{bmatrix} 1 & 0 \\ 0 & \exp(i\frac{\pi}{2}) \end{bmatrix}$$


$$U_{\pi/2} = \begin{bmatrix} 1 & 0 \\ 0 & i \end{bmatrix}$$

- **$\pi/8$  Gate.** A  $\pi/8$  Gate Operator can be represented by using  $\theta = \pi/4$ ,  $\phi = \pi/8$  and  $\hat{n} = (0, 0, 1)$

$$U_{\pi/8} = e^{i\frac{\pi}{8}} R_z\left(\frac{\pi}{4}\right) = e^{i\frac{\pi}{8}} \begin{bmatrix} \exp(-i\frac{\pi}{8}) & 0 \\ 0 & \exp(i\frac{\pi}{8}) \end{bmatrix} = \begin{bmatrix} 1 & 0 \\ 0 & \exp(i\frac{\pi}{4}) \end{bmatrix}$$

We can realize these gates in our system by coupling a two-level system to an external EM field [23, 24]. Let us write the state of the atom as follows:

$$\psi(t) = C_0(t) |\psi_0\rangle + C_1(t) |\psi_1\rangle$$

where  $|\psi_n\rangle$  are the energy eigenstates of the atoms that are relevant to the computational scheme ,  $C_0(t) = e^{-E_n t/\hbar} C_0(0)$  are the complex amplitude, and  $E_n = \hbar\omega_n$  are the eigenvalues. We write the Hamiltonian as

$$H = H_0 + V(t)$$

where  $H_0$  is the free Hamiltonian, and  $V(t)$  is the interaction between the electromagnetic field and the atom.

$$V(t) = \mu [A(t) e^{-i\omega t} + A^*(t) e^{i\omega t}]$$

where  $\mu$  is the electric or magnetic moment,  $\omega$  is the EM field frequency, and  $A(t)$  represents the EM



field amplitude, which we can treat classically. We calculate the matrix element as  $\langle \psi_n | V(t) | \psi_m \rangle$

$$V(t) = \begin{bmatrix} 0 & V_{0,1} \\ V_{1,0} & 0 \end{bmatrix}$$

where  $V_{n,m} = -\mu_{n,m} [A(t) e^{-i\omega t} + A^*(t) e^{i\omega t}]$ . Therefore, the Hamiltonian is

$$H = \begin{bmatrix} E_0 & V_{0,1} \\ V_{1,0} & E_1 \end{bmatrix}$$

The time-dependent Schrodinger equation for the two-level system is

$$i\hbar \frac{\partial \psi}{\partial t} = H\psi$$

$$i\hbar \frac{d}{dt} \begin{pmatrix} B_0(t) \\ B_1(t) \end{pmatrix} = \begin{pmatrix} \omega_0 & V_{0,1}/\hbar \\ V_{1,0}/\hbar & \omega_1 \end{pmatrix} \begin{pmatrix} B_0(t) \\ B_1(t) \end{pmatrix}$$

by transform the amplitudes  $B_i(t) = C_i(t) e^{-i\omega_i t}$  we can obtain

$$i\hbar \frac{d}{dt} \begin{pmatrix} C_0(t) \\ C_1(t) \end{pmatrix} = \begin{pmatrix} 0 & -\mu [A(t) e^{-i\omega t} + A^*(t) e^{i\omega t}] e^{-i\omega_{10} t} \\ -\mu [A(t) e^{-i\omega t} + A^*(t) e^{i\omega t}] e^{-i\omega_{10} t} & 0 \end{pmatrix} \begin{pmatrix} C_0(t) \\ C_1(t) \end{pmatrix}$$

where  $\omega_{10} = \omega_1 - \omega_0$ . In the rotating wave approximation, the terms that oscillate quickly are dropped, and the term that rotate slowly remains.

$$i\hbar \frac{d}{dt} \begin{pmatrix} C_0(t) \\ C_1(t) \end{pmatrix} = \begin{pmatrix} 0 & \frac{\Omega^*}{2} e^{i\delta t} \\ \frac{\Omega}{2} e^{-i\delta t} & 0 \end{pmatrix} \begin{pmatrix} C_0(t) \\ C_1(t) \end{pmatrix}$$

where  $\delta = \omega - \omega_{01}$  is the detuning of the EM field from resonance, and  $\Omega = 2\mu A/\hbar$  is the Rabi frequency.

In the resonant case, the evolution of the Bloch vector in the presence of an external pulse (Rabi

pulse) can be described [24]

$$u(t) = \begin{pmatrix} 1 & 0 & 0 \\ 0 & \cos \theta(t) & \sin \theta(t) \\ 0 & -\sin \theta(t) & \cos \theta(t) \end{pmatrix} u_0$$

where  $\theta(t) = \int_0^t \sqrt{|\Omega(t')|^2 + \delta^2} dt'$ . Namely, the Rabi pulse rotates the Bloch vector about the x axis. In the state vector representation, a resonant pulse of duration t is expressed by the application of a unitary operator  $U(t)$  to the state vector:

$$|\psi(t)\rangle = U(\hat{t}) |\psi_0\rangle$$

$$U(\hat{t}) = \begin{pmatrix} \cos \frac{\theta(t)}{2} & i \sin \frac{\theta(t)}{2} \\ -i \sin \frac{\theta(t)}{2} & \cos \frac{\theta(t)}{2} \end{pmatrix} \quad (3)$$

by setting the angle  $\theta(t)$  can obtain the one qubit gate. This can be done with coils that create magnetic field with  $\omega_1$  in this case, the Rabi frequency is given by  $\Omega = \mu B/\hbar$  and the detuning is  $\delta = \omega_1 - \omega_0$ .

For example, by taking EM pulse as  $\theta(t) = \pi/2$

$$U(\hat{t})_{\pi/2} = \frac{1}{\sqrt{2}} \begin{pmatrix} 1 & i \\ -i & 1 \end{pmatrix}$$

If the atom is initially prepared in one of the basis states, a  $\pi/2$  pulse transforms it into a superposition state

$$|0\rangle \rightarrow \frac{1}{\sqrt{2}} (|0\rangle + i|1\rangle) \quad |1\rangle \rightarrow \frac{1}{\sqrt{2}} (|1\rangle - i|0\rangle)$$

Therefore, by taking RF pulse with detuning relevant as  $|0\rangle$  or  $|1\rangle$ , we can drive the atom state with Phase gate,  $\pi/8$ , gate and Hadamard gate.

**Two-qubit gate.** To implement the two-qubit  $\sqrt{\text{SWAP}}$  gate, we utilize two unique advantages of ultracold atoms.

- Ability to control the interaction between atoms around Feshbach resonance [19].
- Ability to shape the potential landscape using far off resonance light, controlling the atom tunneling between two traps [18].

These, together with fermionic statistics, are the basis for a new protocol for  $\sqrt{\text{SWAP}}$  gate. This protocol is original but similar in some aspects to the gate first described in [15]. We consider two optical microtraps with one atom at each site, with a distance  $d$  between them. Using second quantization and the Fermi-Hubbard model [26], the Hamiltonian is given by

$$\begin{aligned} H_{J,U} &= J \left( \hat{u}_1^\dagger \hat{u}_2 + \hat{u}_2^\dagger \hat{u}_1 + \hat{d}_1^\dagger \hat{d}_2 + \hat{d}_2^\dagger \hat{d}_1 \right) + 2U \left( \hat{u}_1^\dagger \hat{u}_1 \hat{d}_1^\dagger \hat{d}_1 + \hat{u}_2^\dagger \hat{u}_2 \hat{d}_2^\dagger \hat{d}_2 \right) \\ &\equiv J \cdot H_J + U \cdot H_u \end{aligned}$$

Where  $J$  is the tunneling energy,  $U$  is on site interaction energy,  $\hat{u}_i$  and  $\hat{u}_i^\dagger$  are annihilation and creation operators of particle  $i$  in state “up”, i.e.,  $|1\rangle$  and  $\hat{d}_i$  and  $\hat{d}_i^\dagger$  are annihilation and creation operators of particle  $i$  in state “down”, i.e.,  $|0\rangle$  with the usual fermionic commutation relations [27].

We assume only on-site interactions because of the short-range interaction atoms e.g.,  $^{40}\text{K}$ .

First, the operation of the  $\sqrt{\text{SWAP}}$  gate in three steps is as follows. At each step, the Hamiltonian is time independent and the unitary evolution operator has the form

$$\hat{U} = e^{-\frac{i}{\hbar} H \cdot t}$$

The  $\sqrt{\text{SWAP}}$  gate can be divided into

$$\hat{U}_{\sqrt{\text{SWAP}}} = e^{-\frac{i}{\hbar} J \cdot H_J \cdot t_1} e^{-\frac{i}{\hbar} U \cdot H_u \cdot t_2} e^{-\frac{i}{\hbar} J \cdot H_J \cdot t_1} \quad (4)$$

where  $t_1 = \frac{\pi\hbar}{4J}$  and  $t_2 = \frac{\pi\hbar}{4U}$ . To prove this relation, we need to calculate the time evolution of  $H_J$  and  $H_U$ .

For  $H_J$  we note that

$$\begin{aligned} H_J \left( \hat{d}_1^\dagger \hat{u}_2^\dagger - \hat{u}_1^\dagger \hat{d}_2^\dagger \right) |0\rangle &= 2J \left( \hat{d}_1^\dagger \hat{u}_1^\dagger + \hat{d}_2^\dagger \hat{u}_2^\dagger \right) |0\rangle \\ H_J \left( \hat{d}_1^\dagger \hat{u}_1^\dagger + \hat{d}_2^\dagger \hat{u}_2^\dagger \right) |0\rangle &= 2J \left( \hat{d}_1^\dagger \hat{u}_2^\dagger + \hat{d}_2^\dagger \hat{u}_1^\dagger \right) |0\rangle \end{aligned} \quad (5)$$

$$\begin{aligned} H_J \left( \hat{d}_1^\dagger \hat{u}_2^\dagger + \hat{u}_1^\dagger \hat{d}_2^\dagger \right) |0\rangle &= 0 \\ H_J \left( \hat{u}_1^\dagger \hat{u}_2^\dagger \right) |0\rangle &= 0 \\ H_J \left( \hat{d}_1^\dagger \hat{d}_2^\dagger \right) |0\rangle &= 0 \end{aligned} \quad (6)$$

Now we look at equations (5) and obtain a simple matrix


$$i\hbar \frac{d}{dt} \begin{bmatrix} A_1(t) \\ A_2(t) \end{bmatrix} = \begin{bmatrix} 0 & 2J \\ 2J & 0 \end{bmatrix} \begin{bmatrix} A_1(t) \\ A_2(t) \end{bmatrix} \quad (7)$$

Where  $A_1(t)$  and  $A_2(t)$  are the amplitude of the time-dependent states, i.e.,  $A_1(t) \left( \hat{d}_1^\dagger \hat{u}_2^\dagger - \hat{u}_1^\dagger \hat{d}_2^\dagger \right) |0\rangle + A_2(t) \left( \hat{d}_1^\dagger \hat{u}_1^\dagger + \hat{d}_2^\dagger \hat{u}_2^\dagger \right) |0\rangle$ . The solutions to equation 7 are as follows:


$$A_1(t) = A \cos \left( \frac{2J}{\hbar} (t - t_0) \right) \quad A_2(t) = A \sin \left( \frac{2J}{\hbar} (t - t_0) \right)$$

Now, we add the solution of equations 6 (homogeneous solution), and we get that the general solution as

$$\begin{aligned} |\psi\rangle &= (C_{00} \hat{d}_1^\dagger \hat{d}_2^\dagger + C_{11} \hat{u}_1^\dagger \hat{u}_2^\dagger + C_{12} \left( \hat{d}_1^\dagger \hat{u}_2^\dagger + \hat{u}_1^\dagger \hat{d}_2^\dagger \right) + \\ &+ A_{12} \left[ \cos \left( \frac{2J}{\hbar} (t - t_0) \right) \left( \hat{d}_1^\dagger \hat{u}_2^\dagger - \hat{u}_1^\dagger \hat{d}_2^\dagger \right) - i \sin \left( \frac{2J}{\hbar} (t - t_0) \right) \left( \hat{d}_1^\dagger \hat{u}_1^\dagger + \hat{d}_2^\dagger \hat{u}_2^\dagger \right) \right] |0\rangle \end{aligned}$$

Where  $|\psi\rangle$  is a solution to the time-dependent equation  $i\hbar\frac{d}{dt}|\psi\rangle = H_J|\psi\rangle$ . Now we can choose,  $C_{11} = C_{12} = C_{00} = 0$  and  $t_0 = 0$   this means that the singlet  $\hat{d}_1^\dagger\hat{u}_2^\dagger - \hat{u}_1^\dagger\hat{d}_2^\dagger$  after  $t_1 = \frac{\pi\hbar}{4J}$  into

$$e^{-i\frac{\pi}{4}H_J} \rightarrow -i\left(\hat{d}_1^\dagger\hat{u}_1^\dagger + \hat{d}_2^\dagger\hat{u}_2^\dagger\right).$$

Now we find the solution for  $t$  

$$\begin{aligned} H_u\left(\hat{d}_1^\dagger\hat{u}_1^\dagger - \hat{u}_2^\dagger\hat{d}_2^\dagger\right)|0\rangle &= 2U\left(\hat{d}_1^\dagger\hat{u}_1^\dagger - \hat{u}_2^\dagger\hat{d}_2^\dagger\right)|0\rangle \\ H_u\left(\hat{u}_2^\dagger\hat{u}_1^\dagger\right)|0\rangle &= 0 \quad H_u\left(\hat{d}_2^\dagger\hat{u}_1^\dagger\right)|0\rangle = 0 \\ H_u\left(\hat{d}_1^\dagger\hat{u}_2^\dagger\right)|0\rangle &= 0 \quad H_u\left(\hat{d}_2^\dagger\hat{d}_1^\dagger\right)|0\rangle = 0 \end{aligned}$$

Here, the solution is simple, because all the single-particle states are stationary, while the solution for the state  $|\psi_0\rangle = \left(\hat{d}_1^\dagger\hat{u}_1^\dagger + \hat{d}_2^\dagger\hat{u}_2^\dagger\right)$  reads

$$|\psi_+\rangle = e^{2it}|\psi_0\rangle \quad (8)$$

Now, we can calculate eq.(4). The first term with  $t = t_1$  is

$$|0_1\rangle = e^{-i\frac{\pi}{4}H_J}|0_{\text{initial}}\rangle$$

We can see that due to the Pauli principle, all the three symmetric states  $\hat{d}_1^\dagger\hat{u}_2^\dagger$ ,  $\hat{u}_2^\dagger\hat{u}_1^\dagger$ ,  $\left(\hat{d}_1^\dagger\hat{u}_2^\dagger + \hat{d}_2^\dagger\hat{u}_1^\dagger\right)$  are stationary in time eq.(6). The singlet state, which is anti-symmetric, evolves as follows:  $\hat{d}_1^\dagger\hat{u}_2^\dagger - \hat{u}_1^\dagger\hat{d}_2^\dagger \xrightarrow{H_J} \hat{d}_1^\dagger\hat{u}_2^\dagger + \hat{u}_1^\dagger\hat{d}_2^\dagger$ . Therefore, at the end of the first evolution, the symmetric states are unchanged, while the anti-symmetric state becomes a state of “two particle” (i.e., doublon  $-i\left(\hat{d}_1^\dagger\hat{u}_1^\dagger + \hat{u}_2^\dagger\hat{d}_2^\dagger\right)$ ). The second evolution with  $t = t_2$  (due to eq. 8)

$$|0_2\rangle = e^{-\frac{i}{\hbar}U\cdot H_u\cdot t_2}|0_1\rangle$$

the “two particle” state obtains a phase of  $e^{-i\pi/2} = -i$  and transforms it into  $-(\hat{d}_1^\dagger \hat{u}_1^\dagger + \hat{u}_2^\dagger \hat{d}_2^\dagger)$ . The three symmetric states does not change. Finally, by repeating the first evolution with  $t = t_1$ , the symmetric states are unchanged, and the “doublon” state gets a phase of  $-i$ . Now, it reverts back to an anti-symmetric singlet state



$$\left(\hat{d}_1^\dagger \hat{u}_2^\dagger - \hat{u}_1^\dagger \hat{d}_2^\dagger\right) \xrightarrow{\sqrt{\text{SWAP}}} i \left(\hat{d}_1^\dagger \hat{u}_2^\dagger - \hat{u}_1^\dagger \hat{d}_2^\dagger\right)$$

In conclusion, the three steps give us

- $\hat{d}_1^\dagger \hat{d}_2^\dagger \rightarrow \hat{d}_1^\dagger \hat{d}_2^\dagger$
- $\hat{u}_1^\dagger \hat{u}_2^\dagger \rightarrow \hat{u}_1^\dagger \hat{u}_2^\dagger$
- $\hat{d}_1^\dagger \hat{u}_2^\dagger + \hat{u}_1^\dagger \hat{d}_2^\dagger \rightarrow \hat{d}_1^\dagger \hat{u}_2^\dagger + \hat{u}_1^\dagger \hat{d}_2^\dagger$
- $\hat{d}_1^\dagger \hat{u}_2^\dagger - \hat{u}_1^\dagger \hat{d}_2^\dagger \rightarrow i \left(\hat{d}_1^\dagger \hat{u}_2^\dagger - \hat{u}_1^\dagger \hat{d}_2^\dagger\right)$

Therefore, combing these three actions together is equivalent to a  $\sqrt{\text{SWAP}}$  gate. In matrix notation,

- $\hat{d}_1^\dagger \hat{d}_2^\dagger \rightarrow \hat{d}_1^\dagger \hat{d}_2^\dagger$
- $\hat{u}_1^\dagger \hat{u}_2^\dagger \rightarrow \hat{u}_1^\dagger \hat{u}_2^\dagger$
- $\hat{d}_1^\dagger \hat{u}_2^\dagger = \frac{1}{2} \left(\hat{d}_1^\dagger \hat{u}_2^\dagger + \hat{u}_1^\dagger \hat{d}_2^\dagger + \hat{d}_1^\dagger \hat{u}_2^\dagger - \hat{u}_1^\dagger \hat{d}_2^\dagger\right) \rightarrow$   
 $\frac{1}{2} \left(\hat{d}_1^\dagger \hat{u}_2^\dagger + \hat{u}_1^\dagger \hat{d}_2^\dagger + i \left(\hat{d}_1^\dagger \hat{u}_2^\dagger - \hat{u}_1^\dagger \hat{d}_2^\dagger\right)\right) = \frac{1+i}{2} \hat{d}_1^\dagger \hat{u}_2^\dagger + \frac{1-i}{2} \hat{u}_1^\dagger \hat{d}_2^\dagger$
- $\hat{u}_1^\dagger \hat{d}_2^\dagger = \frac{1}{2} \left(\hat{d}_1^\dagger \hat{u}_2^\dagger + \hat{u}_1^\dagger \hat{d}_2^\dagger - \hat{d}_1^\dagger \hat{u}_2^\dagger + \hat{u}_1^\dagger \hat{d}_2^\dagger\right) \rightarrow$   
 $\frac{1}{2} \left(\hat{d}_1^\dagger \hat{u}_2^\dagger + \hat{u}_1^\dagger \hat{d}_2^\dagger - i \left(\hat{d}_1^\dagger \hat{u}_2^\dagger - \hat{u}_1^\dagger \hat{d}_2^\dagger\right)\right) = \frac{1-i}{2} \hat{d}_1^\dagger \hat{u}_2^\dagger + \frac{1+i}{2} \hat{u}_1^\dagger \hat{d}_2^\dagger$

which is the same as the matrix form  that I showed above in equation . We can simplify the gate in two additional step or one additional step. We note that

$$H_{J,U} \left(\hat{d}_1^\dagger \hat{u}_2^\dagger - \hat{u}_1^\dagger \hat{d}_2^\dagger\right) |0\rangle = 2J \left(\hat{d}_1^\dagger \hat{u}_1^\dagger + \hat{d}_2^\dagger \hat{u}_2^\dagger\right) |0\rangle$$

$$H_{J,U} \left(\hat{d}_1^\dagger \hat{u}_1^\dagger + \hat{d}_2^\dagger \hat{u}_2^\dagger\right) |0\rangle = 2J \left(\hat{d}_1^\dagger \hat{u}_2^\dagger - \hat{u}_1^\dagger \hat{d}_2^\dagger\right) |0\rangle + 2U \left(\hat{d}_1^\dagger \hat{u}_1^\dagger + \hat{d}_2^\dagger \hat{u}_2^\dagger\right) |0\rangle$$

Now we can write these equations in a matrix form

$$i\hbar \frac{d}{dt} \begin{bmatrix} A_1(t) \\ A_2(t) \end{bmatrix} = \begin{bmatrix} 0 & 2J \\ 2J & 2U \end{bmatrix} \begin{bmatrix} A_1(t) \\ A_2(t) \end{bmatrix} \quad (9)$$

Where the matrix eigenvalues are:

$$\lambda_{1,2} = U \pm \sqrt{4J^2 + U^2}$$

and the eigenvectors are as follows:

$$V_{1,2} = \frac{1}{2J} \begin{bmatrix} -\lambda_{2,1} \\ 2J \end{bmatrix}$$

Thus, the solution is given by  $Ae^{-i\lambda_1 t} V_1 + Be^{-i\lambda_2 t} V_2$  and  $AV_1 + BV_2 = \begin{bmatrix} 1 \\ 0 \end{bmatrix}$ . The second-term solution is  $A = -B$ . Therefore, the solution for the amplitude, equation 9, is

$$\begin{aligned} &= \frac{Ae^{-i\frac{U}{\hbar}t}}{2J} \left( e^{-i\frac{t}{\hbar}\sqrt{4J^2+U^2}} \begin{bmatrix} -U + \sqrt{4J^2 + U^2} \\ 2J \end{bmatrix} - e^{i\frac{t}{\hbar}\sqrt{4J^2+U^2}} \begin{bmatrix} -U - \sqrt{4J^2 + U^2} \\ 2J \end{bmatrix} \right) = \\ &= Ae^{-i\frac{U}{\hbar}t} \begin{bmatrix} \frac{\sqrt{4J^2+U^2}}{J} \cos\left(\frac{t}{\hbar}\sqrt{4J^2 + U^2}\right) + i\frac{U}{J} \sin\left(\frac{t}{\hbar}\sqrt{4J^2 + U^2}\right) \\ -2i \sin\left(\frac{t}{\hbar}\sqrt{4J^2 + U^2}\right) \end{bmatrix} \quad (10) \end{aligned}$$

We can find a specific solution if we choose the parameter correctly.

$$\frac{t^*U}{\hbar} = \frac{\pi}{2}(4n-1) \quad \frac{t^*}{\hbar}\sqrt{4J^2 + U^2} = \pi m \quad (11)$$

Where  $m$  is an odd integer and  $n$  is any integer.

By using these choices, equation 11 and  $A = \frac{\sqrt{m^2 - (2n - 1/2)^2}}{2m}$  (the solution should be normalized), we obtain equation

$$\begin{bmatrix} A_1(t^*) \\ A_2(t^*) \end{bmatrix} = i \begin{bmatrix} 1 \\ 0 \end{bmatrix} \quad (12)$$

From equation 12, we obtain the  $\sqrt{\text{SWAP}}$  gate.

$$\begin{pmatrix} \hat{d}_1^\dagger \hat{u}_2^\dagger - \hat{u}_1^\dagger \hat{d}_2^\dagger \\ \hat{d}_1^\dagger \hat{u}_1^\dagger + \hat{d}_2^\dagger \hat{u}_2^\dagger \end{pmatrix} \xrightarrow{\sqrt{\text{SWAP}}} \begin{pmatrix} i(\hat{d}_1^\dagger \hat{u}_2^\dagger - \hat{u}_1^\dagger \hat{d}_2^\dagger) \\ 0 \end{pmatrix}$$

From these two equations, (11), we can obtain the strength of the interaction  $U$  and the time  $t$  for which the interaction acts similar to  $\sqrt{\text{SWAP}}$  gate

$$U = \pm \frac{2J\hbar(2n - \frac{1}{2})}{\sqrt{m^2 - (2n - \frac{1}{2})^2}} \quad t = \frac{\hbar\pi\sqrt{m^2 - (2n - \frac{1}{2})^2}}{2J} \quad (13)$$

The last parameter,  $J$ , depends on the distance between the two qubits, i.e.,  $d(t)$ . One of our goals is to optimize  $d(t)$ .

#### 2.1.4 Ability to Measure the Results

In our system, we can detect the population of state  $|0\rangle$  ( $|-9/2, -9/2\rangle$ ) in a fluorescence imaging using the cycling transition  $|-9/2, -9/2\rangle \rightarrow |11/2, -11/2\rangle$ . Unfortunately, we cannot detect the cycling transition  $|-9/2, -9/2\rangle \rightarrow |11/2, -11/2\rangle$  in our platform. The typical trap depth is  $\sim 400$  nK, and the recoil temperature in  $^{40}\text{K}$  is 404 nK [28]; therefore, the atom drives out from the trap (even when the direction is random and the heating goes as  $\sqrt{N_{\text{photon}}}$ ). To overcome this problem, we can measure it with a Raman sideband cooling technique [29] (for more details, see section 3.2). Recent studies with  $^{40}\text{K}$  sideband cooling have shown that single atoms release approximately 60 photom/sec [14, 15]. Consequently, we can collect 10% of the photons, and it uses the ability to measure one-atom fluorescence with the CCD camera (depending on the objective solid fraction angle and the laser



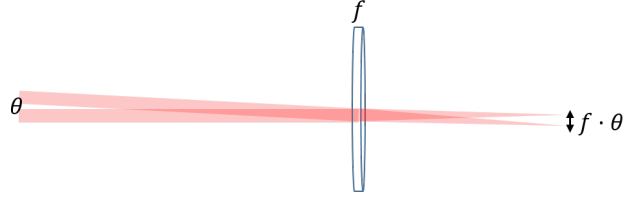


Figure 3: The distance between two traps that reach the lens with an angle  $\theta$ .

detuning equation 18). Shorter detection times can tune the probe laser frequency and raise the microtraps depth.

### 2.1.5 Scalability

In our system, the scalability is straight forward. When one qubit can be initiated and controlled, adding more microtraps, you can obtain a larger number of qubits. The other microtraps are created by other laser beams that reach the optical objective. These lasers are then focused to different positions at the focal plane:

$$d = f \cdot \theta$$

Where  $d$  is the distance between two microtraps,  $f$  is the objective focal length, and  $\theta$  is the angle between the incoming beams (see figure 3). One way to do it dynamically is by employing two Acousto-Optic-Modulators (AOM), one in  $x$  axis and one in  $y$  axis [30]. We can position the qubits with  $d \gg \lambda$  and then  $J \approx 0$ . Then, the qubits can be brought closer with the optimal  $d(t)$ . For one-qubit gates, we can take one qubit to a position where the RF field is optimal and far enough from other qubits (see 4).

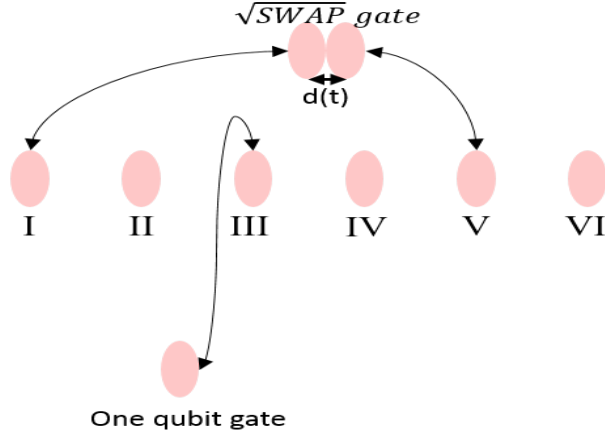


Figure 4: Array of qubits that are formed by two AOMs. The qubits are moved to the  $\sqrt{SWAP}$  region (I & V atoms) or to the one-qubit gate region (III atom) according to the quantum code.

The qubit isolation depends on the lifetime in the optical microtrap. We can reduce the laser power when the atom state is at the ground state and obtain a lifetime of several minutes (see more details see section 3.4 ). Therefore, the decoherence in our system should be very slow. Furthermore, in our method, we can find  $m$  and  $n$  (eq.13) such that  $\mathcal{F} \rightarrow 1$  (the fidelity is the overlap between the chosen target state and the spin state as measured or calculated  $\mathcal{F} = \langle \psi_{\text{target}} | \hat{\rho} | \psi_{\text{target}} \rangle$ ).

## 2.2 Theoretical simulation and calculation

To make a numerical calculation of a single atom in a microtrap, we need to solve the time independent Schrodinger equation that is given by

$$H\psi(r, \theta, z) = E_n\psi(r, \theta, z) \tag{14}$$

where  $E_n$  is the state energy of state  $n$  and  $H$  is the system Hamiltonian given by

$$H = -\frac{\hbar^2}{2m}\nabla^2 + V(r, \theta, z)$$

where  $V$  is the potential. In 3D potential of a single microtrap is

$$V(r, z) = -V_0 \frac{\omega_0^2}{\omega(z)^2} e^{-2\frac{r^2}{\omega(z)^2}}$$

where  $\omega(z) = \omega_0 \sqrt{1 + \left(\frac{z\lambda}{\pi\omega_0^2}\right)^2}$ . The waist of a Gaussian beam is given by  $\omega_0 = \frac{\lambda}{\pi \cdot NA}$ , where  $NA$  is the numerical aperture. The trap parameters are laser beams with  $NA = 0.9$  and  $\lambda = 1064$  nm. We calculated the eigenenergies and the eigenstates by solving numerically [4]. The numerical 2D calculation takes advantage of the cylindrical symmetry with 112 divisions in the radial direction and 102 divisions in the axial direction, and the accuracy of the results is better than 1%. The result of the calculation is shown in Figure 5. We present calculations in low-optical trap  $V_0/k_B = 310$  nK to obtain bound symmetric eigenstates (in other word, laser with power of  $1.06 \mu\text{W}$ ). In this optical depth regime can get lifetime of  $\sim 438$  sec (more details in 3.4). Figure 6 shows the plots of the bound states in a single Gaussian potential for  $m = 0, 1$  ( $m$  is the azimuthal quantum number). We can see that for lower  $NA$  need to low the optical trap depth and the lowest eigenenergy depth is smaller. In figure 6 we can see that for one bound symmetric eigenstate we need a low depth optical trap ( $NA=0.9$ ).

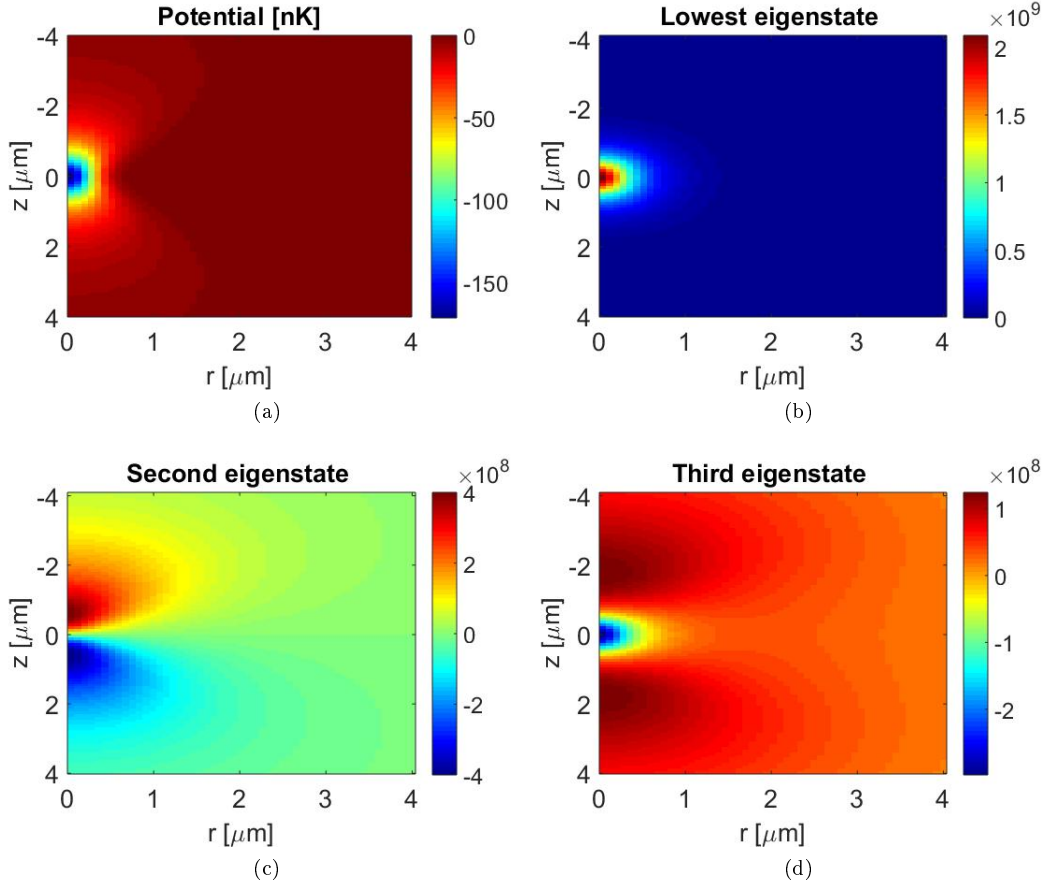


Figure 5: Calculations of bound states in a single Gaussian potential. a) Potential of one trap with  $\text{NA}=0.9$  and  $V_0/k_b = 310$  nK at  $y = 0$ . b) Lowest eigenstate (symmetric) with energy  $E/k_b \approx -40$  nK. c) Second eigenstate with energy  $E/k_b \approx -1.5$  nK (antisymmetric). d) Third eigenstate with energy  $E/k_b \approx -0.316$  nK (symmetric). Other states have  $E/k_b > 0$  and are therefore not bound.

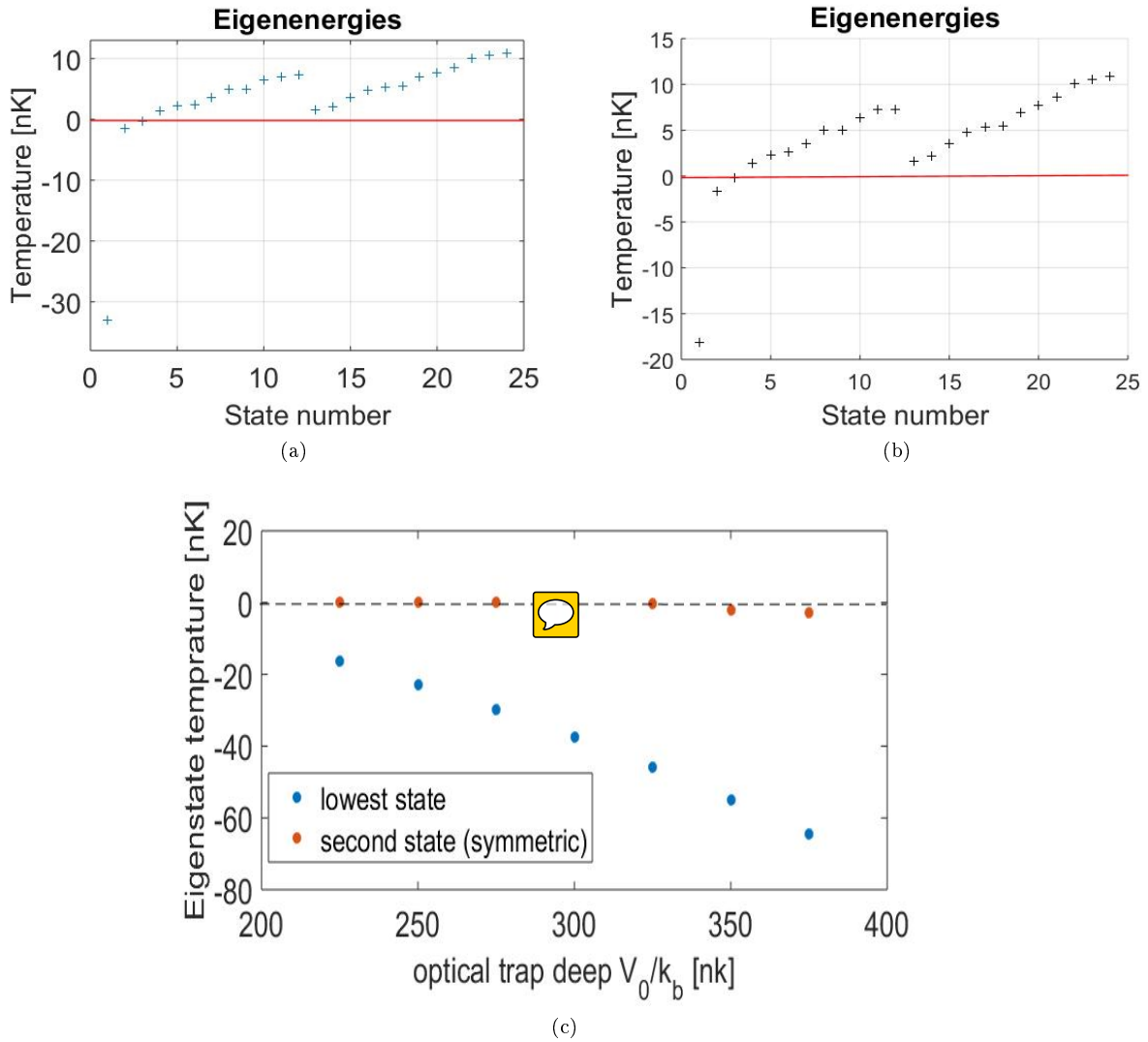


Figure 6: a) Calculations of bound states in a single Gaussian potential with  $NA=0.9$ . The first 12 are with  $m = 0$  and the next 12 with  $m = 1$ . There are three bound states ( $E < 0$ ) that are plotted in Figure 5b, Figure 5c, and Figure 5d. b) Calculations of bound states in a single Gaussian potential with experimentally condition  $NA=0.75$ . Here  $E_1 = -18.14$  nK,  $E_2 = -1.67$  nK  $E_3 = -0.16$  nK. c) Lowest and second eigenstates energy (in terms of temperature) vs. optical trap depth.

In order to solve numerically the problem of two atoms in two traps with distance  $d(t)$  we need to solve the time-dependent Schrodinger equation for two particles. This is one of the theory calculation that need to be done. but first we can solve the problem with one atom in two Gaussian traps

that separated with a constant  $d$ . By knowing the energy difference between the symmetric and the antisymmetric state we can state we can to define  $J$  ( $\Delta E \approx 2J$ ). In figure 7 I show the eigenenergy of this system with  $d = 0.8 \cdot \lambda$  and  $NA=0.9$ . The energy difference is  $\Delta E = 4.968 \cdot 10^{-31}$  J and the  $\sqrt{SWAP}$  gate time is  $T_g \sim 0.3$  ms (eq. 13). On the other hand, the scattering rate is given by eq. 19. I calculate the lifetime in the trap  $T_I = (\frac{\Gamma}{\hbar} V_0)^{-1} \approx 440$  sec [31]. This give the ratio  $\frac{T_{gate}}{T_I} \sim 10^{-6}$  and it fulfills the decoherence requirement (27).

There are many more numerical calculations that must be preformed, e.g., the gates parameter  $U$ ,  $t$ ,  $d(t)$  (equation 13) for two-qubit gate and one-qubit gate parameters that given by equation 6. Another parameter is the transfer qubit trajectory to obtain a fast transfer [32]. All these parameters need to be optimized with demand on the fidelity  $\mathcal{F} > 0.99$ .

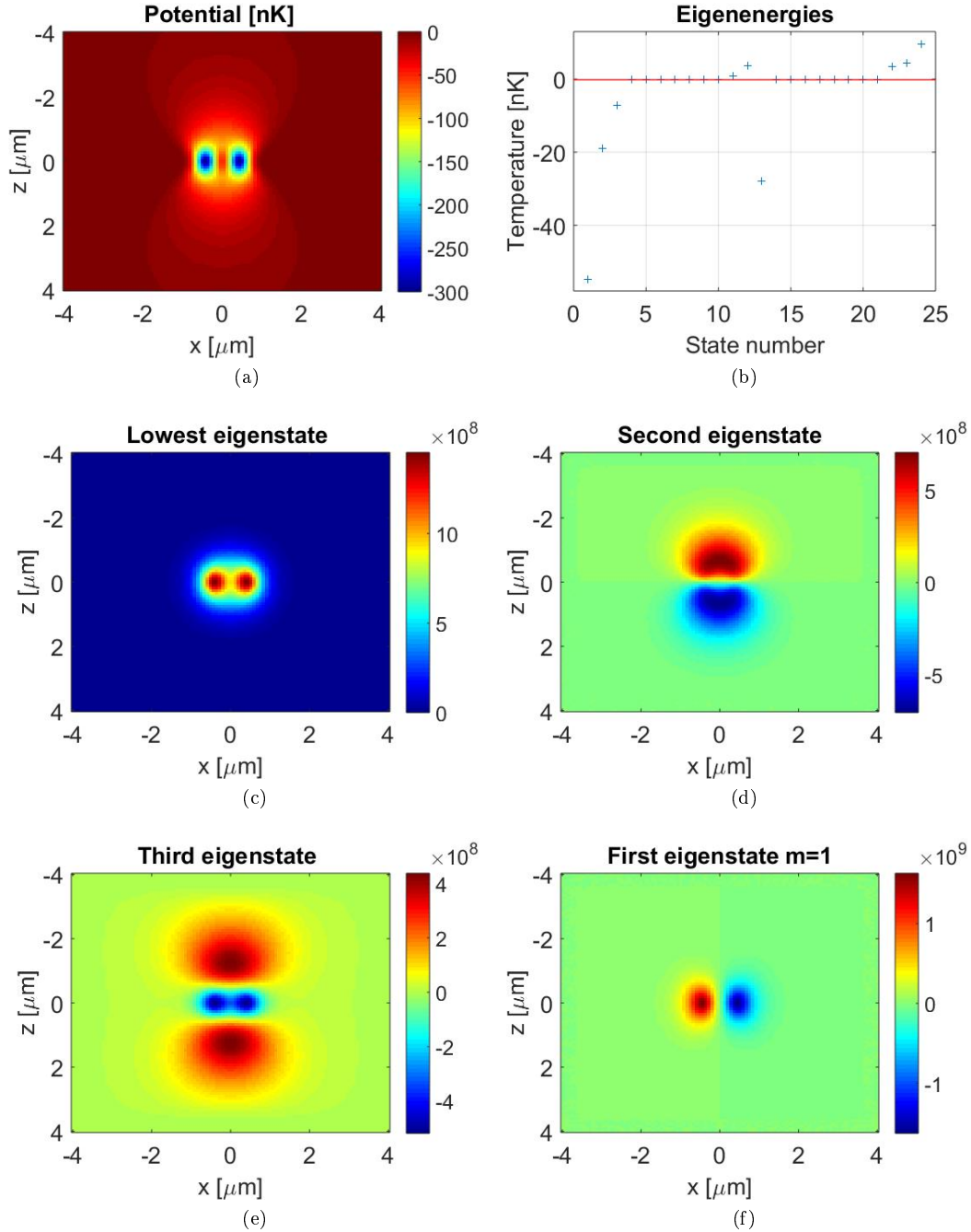


Figure 7: a) Potential of two traps with  $d = 0.8 \cdot \lambda$  at  $y = 0$ . b) Eigenenergies calculations of bound states in a double Gaussian potential. The first 12 is are with  $m = 0$  and the next 12 is with  $m = 1$ . There are four bound states in this potential (with  $E < 0$ ). The lowest state is with  $E = -54.8$  nK and the second bound state with  $E = -18.85$  nK. For this calculation the traps parameters are  $d = 0.8 \cdot \lambda$  with  $\lambda = 1064$  nm, and each trap depth is  $V_0/k_b = 310$  nK and  $NA=0.9$ . This 3D numerical calculation is done in Cartesian coordinates with 102 divisions at each dimension. c) Lowest eigenstate (symmetric) with energy  $E/k_b \approx -54.82$  nK. d) Second eigenstate with energy  $E/k_b \approx -18.85$  nK (antisymmetric in  $z$  axis and symmetric in  $x$  axis). e) Third eigenstate with energy  $E/k_b \approx -7.23$  nK. f) Lowest eigenstate with  $m=1$  and the energy is  $E/k_b \approx -27.94$  nK.

## 3 Ultracold atoms

The field of ultracold atoms has seen rapid development during the last 20 years. Many new experimental techniques have been introduced, and the experimental toolbox has been vastly expanded. Cooling and trapping of atoms is based on the use of forces acting on atoms in laser fields or on the combination of laser fields and magnetic fields. This chapter presents a brief background of cooling and trapping techniques.

### 3.1 Laser cooling technique

#### 3.1.1 Doppler cooling


Doppler cooling mechanism was experimentally described in 1978 [33] and is the basis of our cooling techniques. At low temperature, kinetic energy sets the temperature by

$$\langle E_k \rangle = \frac{3}{2} k_B T$$

where  $k_b$  is a Boltzmann constant. Each time a photon is absorbed by an atom, the atom receives the recoil momentum  $\frac{h\nu}{c}$  in the laser propagation direction. When it emits a photon, it again changes its momentum by the same value but in a random direction. Accordingly, if the atom travels in the opposite direction to the laser propagation direction, the atom slows. However, if the atom moves in the same direction as the laser propagation direction, it accelerates.

To slow down the atom, Doppler cooling takes advantage of the Doppler effect, a shift in frequency for an observer moving relative to its source. This means that as the atom moves, it experiences a shift in laser-beam frequency. When the atom moves towards the laser-beam propagation, it experiences a frequency shift of  $+\delta\nu_D$ , and if it moves in the opposite direction to the laser propagation, the shift is  $-\delta\nu_D$ . Thus, if the laser frequency is lower than the resonance frequency  $\nu_0 - \delta\nu$ , the atom that travels in the same direction as the laser experiences, according to the Doppler effect,  $\nu_0 - \delta\nu + \delta\nu_D$ . In contrast, the atom that travels in the opposite direction experiences  $\nu_0 - \delta\nu - \delta\nu_D$ . Accordingly, the atom that travels in the direction of the laser experiences a force corresponding to the resonance



frequency  $\sim \nu_0$ , while an atom that travels in the opposite direction of the laser experiences a force that corresponds to a frequency that is far of resonance  $\sim \nu_0 - 2\delta\nu$ . Changing the detuning is one way of controlling the magnitude of this force and drastically affects the number of trapped atoms . Therefore, Doppler cooling creates a velocity-dependent force. It slows down atoms selectively based on the magnitude of their velocity.

### 3.1.2 Sisyphus Cooling

Sisyphus cooling (polarization-gradient cooling) is a laser-cooling technique that was observed experimentally and later first given a full explanation by Claude Cohen-Tannoudji [34]. Sisyphus cooling is achieved by two orthogonal polarization laser beams. The two lasers create a polarization lattice. When the atoms move to the maximum of the potential (and the resonance frequency is closer to the laser frequency), they lose kinetic energy and move slower. As they reach the maximum, they are optically pumped to the minimum, as shown in Figure 8a. In  $^{40}\text{K}$ , this technique does not work due to the narrow and inverted hyperfine structure of the  $P_{3/2}$  state [35].

### 3.1.3 Gray Molasses Cooling

Gray Molasses is a cooling technique similar to Sisyphus cooling. The difference between them is that in Gray Molasses, the electromagnetic field splits the energy levels into a dark state and bright states. If the laser beam is blue detuned, the bright level is light-shifted and the dark state does not change (since it is not coupled to the light field). Similar to Sisyphus cooling, the atoms climb to the maximum of the potential well and are then pumped to the dark level (see Figure 8b). As a general principle, a better-cooling scheme is where the coldest atoms are pumped to a dark state and are not heated by spontaneous scattering events. Recent studies [36, 37] have showed that for  $^{40}\text{K}$ , Gray Molasses on the  $D_1$  line can reach a temperature of  $T \sim 15 \mu\text{K}$ .

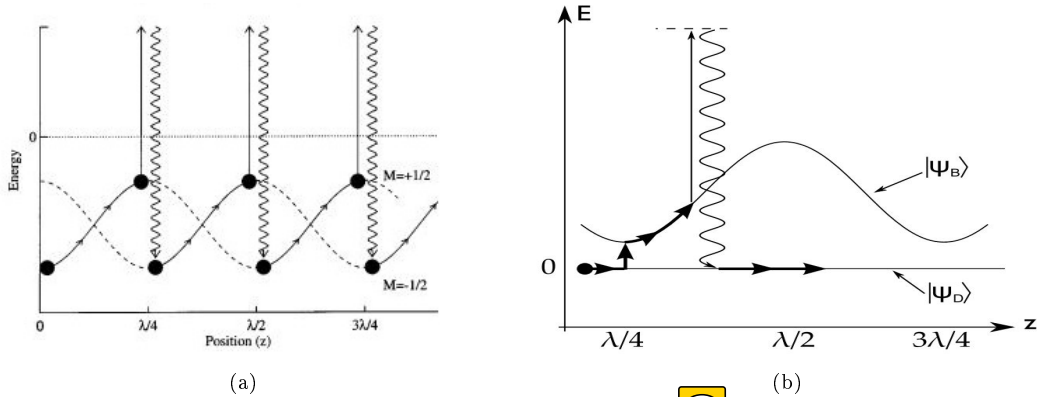


Figure 8: a) Sisyphus cooling scheme. Adopted from ref. [38] b) Gray Molasses cooling scheme. With positive detuning, the ground state splits to two states,  $|\psi_D\rangle$  and  $|\psi_B\rangle$ . These two states act similar to the states in Sisyphus cooling. Adopted from ref.[37].

### 3.1.4 Magneto optical trap

A MOT consists of laser-beam propagation and retro-reflecting along three orthogonal directions and coils with anti-Helmholtz configuration. The laser beams with red-detuning from an energy transition in the potassium spectrum are sent to the atoms. The main mechanism is the Doppler (3.1.1) effect [39]. The red-detuned (light with a frequency smaller than the resonance frequency) light is Doppler shifted in the rest frame of a moving atom. This shift causes the atoms to interact with the laser as if they are moving opposite to the laser propagation direction. We cool the atoms by lowering their velocities. However, in this process, there is a limit [39] to the temperature:

$$T_D = \frac{\hbar\Gamma}{2k_B}$$

where  $k_B$  is the Boltzmann's constant,  $\hbar$  is the reduced Plank's constant, and  $\Gamma$  is the natural line-width. In  $^{40}\text{K}$ , the Doppler limit is  $T_D \sim 150 \mu\text{K}$ .

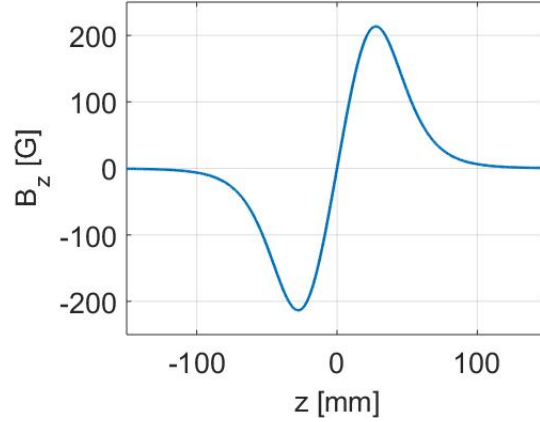


Figure 9: The magnetic field created by anti-Helmholtz configuration

### 3.1.5 Magnetic field for MOT

Doppler cooling lowers the temperature of atoms but does not differentiate between an atom far from the middle of the trap and an atom at the center. A magnetic field takes advantage of the Zeeman effect to localize the atoms and to increase the density. Atoms can have different angular momentum  $m_z = -f, -f + 1, \dots, f$  where  $f$  is the total atomic spin. In the presence of a magnetic field, the energy levels are split into sub-levels. The energy change is given by the following:

$$\Delta U = -\vec{\mu} \cdot \vec{B}$$

where  $\vec{\mu}$  is the magnetic dipole moment of the state and  $\vec{B}$  is the magnetic field. Therefore, the energy difference is proportional to the magnetic field and depends on its direction.

Coils with an anti-Helmholtz configuration produce a magnetic field that switches its sign at the origin (see Figure 9). This gives two regions, positive and negative. At the origin, the magnetic field is zero. Therefore, the energy shift is  $\Delta U \approx 0$ . In the positive magnetic field,  $m_z < 0$  and states have increased energy, while in the negative magnetic field,  $m_z > 0$  and the states have decreased energy. ( $\Delta U$  goes opposite to the magnetic field). Therefore, as shown in Figure 10, a photon with the correct polarization is confined by the atoms, giving a spatially dependent force with zero force in

the center. Figure 11 summarizes the laser directions and polarization in 3D due to the magnetic field from quadratic coils.

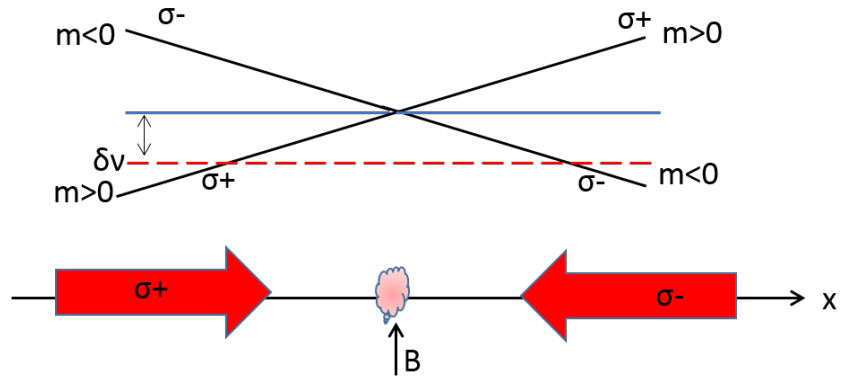


Figure 10: Description of Zeeman split and polarization of laser beams with detuning  $\delta\nu$  in one dimension. The blue line is the energy level at zero magnetic field. On the left, the magnetic field is negative, therefore, the atom interacts with  $\sigma^+$  laser polarity. On the right side, the magnetic field is positive, so the atom interacts with  $\sigma^-$  laser polarity.

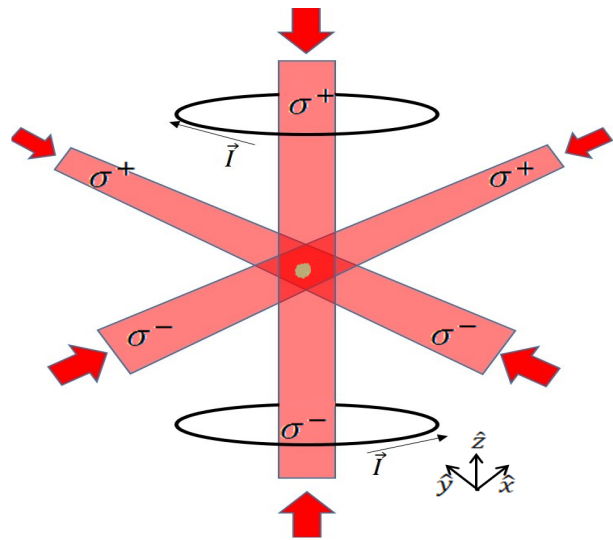


Figure 11: MOT configuration in 3D.

### 3.2 Raman Sideband cooling

To describe Raman sideband cooling, a Raman transition must be explained [40]. A Raman transition is a two-photon transition consisting of absorption and stimulated emission. As shown in Figure 1.1, an atom moving with velocity  $v$  that absorbs a photon with frequency  $\omega_1$  is excited to a virtual state  $|c\rangle$ . Immediately, another photon with frequency  $\omega_2$  traveling in the opposite direction causes stimulated emission of the atom into state  $|b\rangle$ . This allows for the precise selection of atoms with velocities that satisfy the equation

$$\frac{v}{c} = \frac{\omega_0 - (\omega_1 - \omega_2)}{\omega_1 + \omega_2}$$

where  $c$  is the speed of light and  $\hbar\omega_0$  is the transition energy between  $|a\rangle$  and  $|b\rangle$ .

We can use the Raman pulse to transfer an atom with velocity  $v$  from  $|a\rangle \rightarrow |b\rangle$ , and with another laser, we can excite the atom from  $|b\rangle \rightarrow |c\rangle$ . At state  $|c\rangle$ , the width of the velocity distribution is  $\sigma_c(v) \ll \sigma_a(v)$ . Therefore, when the atom decays back to  $|a\rangle$  with velocity around  $v - v_r$ , at the end of the cycle, we have more atoms with lower velocity. In 1995, Wineland *et al.* [23], proposed cooling an atom to the ground state in a 3D-optical trap scheme that was based on Raman transition. Only recently and with more sophistication was [24] formed with  $^{40}\text{K}$  [14] in an optical lattice. By cooling with Raman sideband technique, we gain two benefits. First, we can detect the number of atoms at each site due to their fluorescence, and second, we can lower the atom to the ground state.

### 3.3 Magnetic trap - QUIC configuration

One cooling technique in ultracold atoms experiments is RF evaporation [41]. In this technique, the atoms are loaded to magnetic trap with  $m_z > 0$ , and by using a RF field, the atoms are transferred to a state with  $m_z < 0$ , which is not magnetically confined; therefore, they leave the trap. In this technique, if the minimum of a magnetic field is zero, then the atoms that are closer to the minimum (with low temperature) can flip their spin and be ejected. A QUIC configuration trap [42] is formed by two quadrupole coils and one Ioffe coil. The MOT uses the same coils as the quadrupole trap, so the transfer of atoms from the MOT into the magnetic trap is straightforward. Atoms are loaded into a quadrupole trap and subsequently transferred to an IOFFE-type trap. Figure 1.13 shows that the

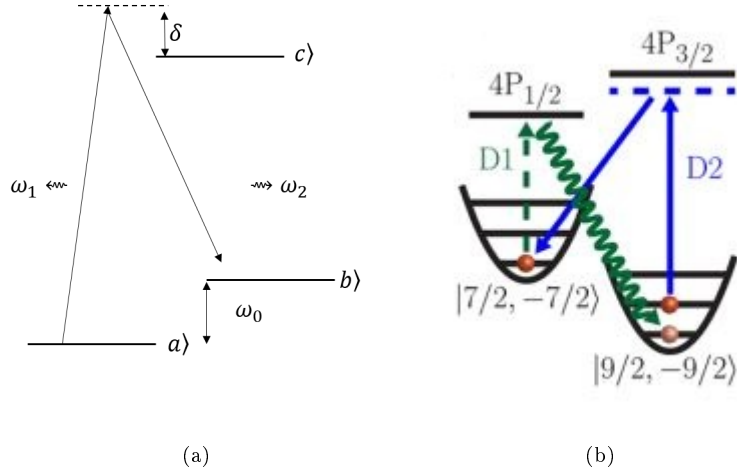


Figure 12: a) Raman transition between two atomic levels  $|a\rangle$  and  $|b\rangle$  b) Raman sideband cooling scheme in  $^{40}\text{K}$  taken from [14].

magnetic field goes from quadrupole with  $\min(B) = 0$  to quadrupole with  $\min(B) = 1$  G, and the minimum is shifted around 17 mm towards the Ioffe coil. The ratio between  $\frac{I}{I_Q}$  depends on the exact sizes of the coils and distance between the quadrupole coils and the Ioffe coil.

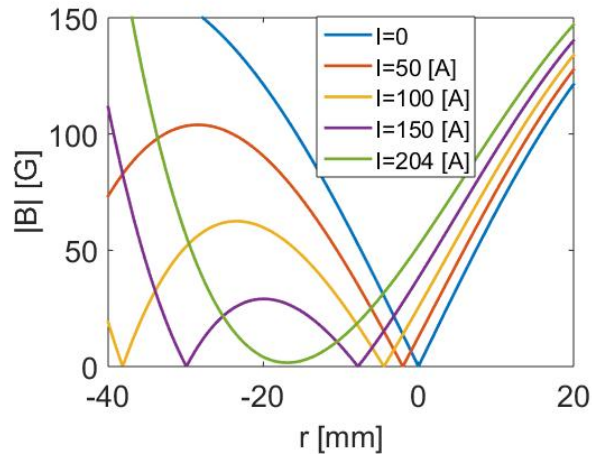



Figure 13: Magnetic field calculations in  $y$  direction starts with quadrupole with  $I_0 = 210$  A and the addition of a Ioffe coil with different current. The minimum is adiabatically moved  $\sim 17$  mm towards the Ioffe coil.

### 3.4 Optical trap

Optical dipole force comes from the potential that an atom feels when the oscillating electric dipole moment of the atom induced by the oscillating electric field of the laser light interacts with the field. Two important quantities for optical dipole traps are the depth of the potential  $U_{dip}(r)$  and the scattering rate  $\Gamma_{sc}(r)$ . In terms of decay rate, they can be expressed as [31]

$$U_{dip}(r) = \frac{3\pi c^2 \Gamma}{2\hbar \omega_0^3 \delta} I(r)$$

$$\Gamma_{sc}(r) = \frac{3\pi c^2 \Gamma^2}{2\hbar^2 \omega_0^3 \delta^2} I(r) \quad (15)$$

where  $I(r)$  is the laser beam intensity,  $\Gamma$  is the natural line-width   $\delta = \omega - \omega_0$  is the frequency detuning of the laser from the frequency of the optical transition  $\omega_0$ . The dipole trap can be attractive for red detuning ( $\delta < 0$ ) or repulsive for blue detuning ( $\delta > 0$ ).

$\lambda$	p [mW]	lifetime [ms]
1064	75	220
820	20	23

Table 2: Comparison of the life time and the laser source power in two commercial laser wavelengths. We required a 1 mK trap that is high enough for atoms at temperature following  $D_1$  cooling ( $T_{D_1} \sim 30 \mu\text{K}$ ).

The simple example is for TEM<sub>00</sub> Gaussian mode far from resonance frequency. Beam intensity is given by

$$I(r, z) = \frac{2P}{\pi \omega^2(z)} e^{-\frac{2r}{\omega^2(z)}}$$

Where  $\omega(z) = \omega_0 \sqrt{1 + \left(\frac{z}{z_R}\right)^2}$ . The peak intensity is given by  $I_0 = 2P/\pi \omega_0^2$ . The trap depth is defined as  $U_0 = |U(0, 0)|$  and is linearly proportional to the beam intensity. Expanding around the

position of maximum intensity leads to a harmonic potential

$$U_{dip}(r, z) = -U_0 \left[ 1 - 2(r/\omega_0)^2 - (z/z_R)^2 \right] \quad (16)$$



## 4 The experimental machines

In our lab, we built an ultracold-atom system with  $^{40}\text{K}$ . This chapter describes the systems and concentrate on the parts I constructed.

### 4.1 The experimental systems

We considered two methods (see sketches in Figure 14) of creating a single atom trapped in an optical trap. Each of these methods has advantages and disadvantages, and we have not yet decided which method to use. We plan to advance in both before making the final decision. Considerations are the preparation time of a single atom trap and the temperature of the atom. The first system includes a machine producing as an initial resource a quantum degenerate Fermi gas with  $T/T_f \ll 1$ . The second method is characterized by loading from only a relatively ultracold cloud after 3D MOT or  $D_1$  cooling, removing all atoms other than one, and then cooling inside the trap.

1. **Degenerate fermi gas.** The first system (see Figure 14a) is composed of three cells under ultrahigh vacuum  $\sim 10^{-11}$  torr. In the first cell (source), we release  $^{40}\text{K}$  atoms from homemade dispensers. The atoms are captured by a 2D MOT. On the third axis, there is a mirror with a hole (nozzle) inside the chamber. The atoms are cooled in two axes and pushed to the second cell by another laser (with different detuning) in the third axis (reflected with hole in the middle by a nozzle). In the second cell (cooling), they are captured and trapped by a 3D MOT. At this point, the cloud temperature is around  $\sim 220 \mu\text{K}$ . By using a Gray Molasses cooling on the  $D_1$  atomic transition, the atomic cloud temperature is reduced to  $\sim 15 \mu\text{K}$ . Next, we optically pump the atoms into the states  $|9/2, 9/2\rangle$  and  $|9/2, 7/2\rangle$  and load the atoms to a magnetic trap with a QUIC configuration [42]. In this configuration, we obtain a magnetic trap without  $B = 0$ . This is important for a RF evaporation. Following the evaporation, the temperature is  $T/T_f \approx 1 - 3$ . Next, we load the atoms to a far-off-resonance optical trap and move the optical trap adiabatically (with air bearing stage) to the science chamber. Then, we first confirm that the cloud is spin polarized and then load it to a microtrap and reduce the trap depth until there is only a single

bound state [18].

The advantages of this approach is that the process of cooling occurs prior to loading, and there is a large spatial separation between the source and the final trap (which ensures a long lifetime of the trapped atom) and a greater density of atoms. The disadvantage is that the process is rather complicated and takes around 80 seconds.

2. **Fast approach.** In the second system (see Figure 14b), we have one cell under high vacuum  $\sim 10^{-11}$  torr. The  $^{40}\text{K}$  atoms is released from a homemade dispenser by heating and trapped with a 3D MOT. Then, by using a Gray Molasses cooling on the  $D_1$  atomic transition, we obtain a cloud with temperature of over dozens of micro-kelvin. Next, we can load directly to a micro-trap made of a far-off-resonance light. Then, using LAC, only a single atom remains trapped. This single atom is "hot" in the sense that its spread over vibration states is large. To measure the atom and cool it to ground state, we plan to use Raman side-band cooling [14, 15].

The advantages of this approach are the simplicity of the apparatus and the short duration of the experiment that allows for a fast data-accumulation rate. The disadvantage is a shorter lifetime due to the residual ambient gas. There is also a possibility to construct a system made of two chambers where one chamber is used with 2D MOT to generate a source.

We are currently building two experimental systems: the first one is a degenerate fermi gas machine where we can proceed with the first approach (this system is planned to be also used for other experiments) and a second smaller system in which we are going to explore the second approach. We started constructing the first system two years ago, and in the meantime, we completed the 2D and 3D MOT,  $D_1$  cooling, optical pumping, magnetic trapping in QUIC trap, RF evaporation, loading into an optical trap, transporting the atoms to the science chamber. We started to build the second system eight months ago (the vacuum chamber was actually evacuated two and a half years ago); we have just one cell we have completed the 3D MOT and are now working on loading atoms to the optical microtrap and detecting them.

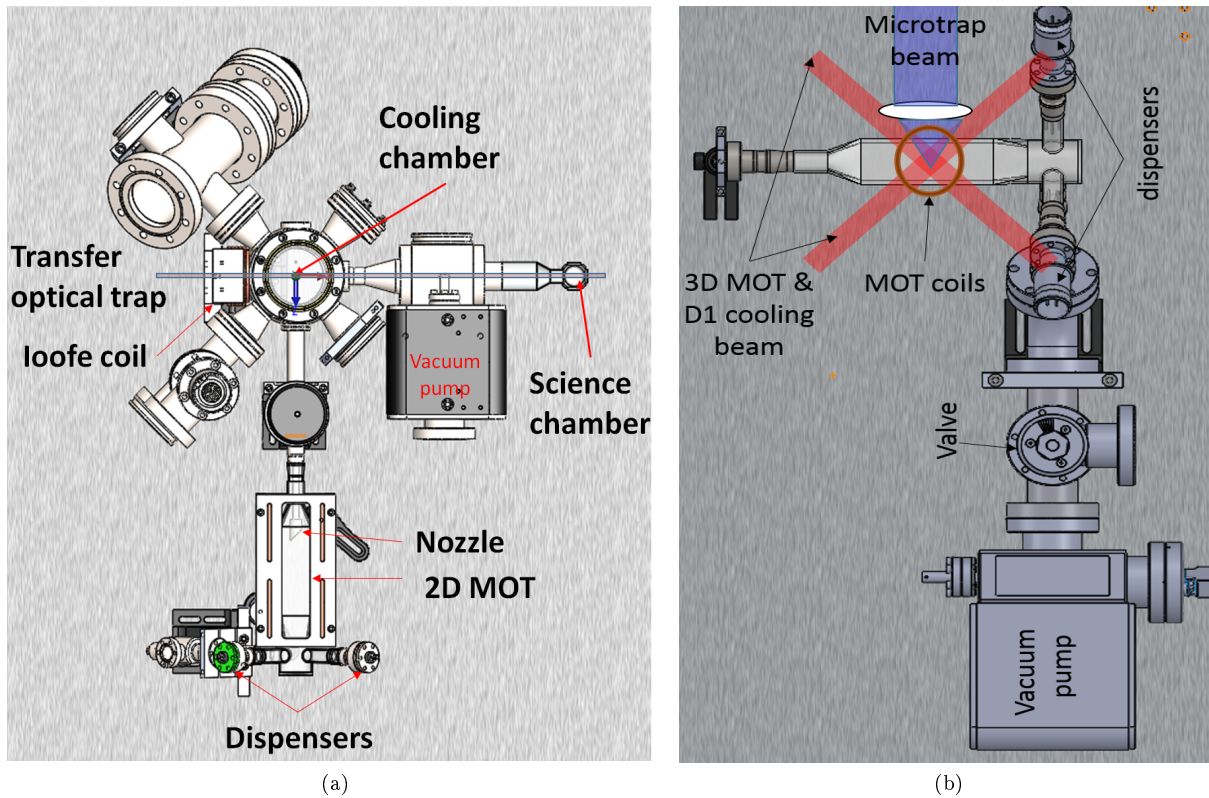


Figure 14: a) Degenerate fermi gas system description. Atoms are released from the dispensers and are trapped by a 2D MOT in the first cell. In the second cell (cooling), atoms are trapped by a 3D MOT and cooled with  $D_1$  cooling and RF evaporation. Then, they are loaded to an optical trap that transfers the atoms to the third cell. b) Fast approach system (with one cell) description. This chamber is similar to the 2D-MOT chamber in the first system. Atoms are released from the dispensers and trapped by 3D MOT. Then, the atoms are loaded into an optical microtrap.

## 4.2 MOT

In both systems the first stage is MOT. In the first method, we start with a 2D MOT and continue to a 3D MOT, and in the fast approach method, we start with a 3D MOT. In the first system, we first used a 2D MOT as described in [43]. For the 3D MOT, we needed, as explained previously, two lasers (cooling and repump) and two coils with anti-Helmholtz configuration. In this configuration, we can not make RF evaporation, as there is a zero-magnetic field at the bottom. Therefore, we added a IOFFE coil in a QUIC configuration [42].

### 4.2.1 Coils setup

Three coils were made from a 4.2X4.2 mm square copper tube, which is hollow to cool the coil at a high current by letting water flow through it. To wrap this coil, we have designed a part made of Teflon that connects to a rotating spindle (15b). Teflon is used so the glue does not stick to the holder and to avoid harming the coating of the coil. After each round, we smeared a layer of glue (*Araldite 2011*) and let it dry for 24 hours.

Considering the dimensions of our system, two coils (both for the 3D MOT and for the magnetic trap) were needed with 7X5 winding with  $r = 20$  mm. Another coil with 6X4 and an inner most radius of  $r = 30$  mm(15a). The coil current is controlled with a Proportional-Integral-Derivative (PID) loop that measures the current by Hall probe.

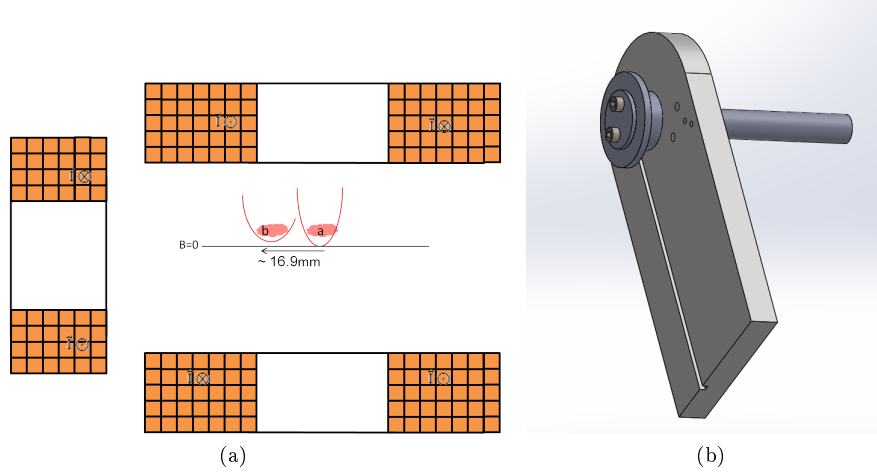



Figure 15: a) QUIC configuration. Atoms are loaded at point a by two coils with anti-Helmholtz configuration with  $U_{\min} = 0$ . When the Ioffe current rises, the atoms are moved to the new minimum, at point b ( $d \sim 16.9$  mm), with  $B_{\min} \approx 1$  G. b) Picture of the part that twisted the coils.

#### 4.2.2 Lasers setup

For MOT, we need two lasers: one laser for cooling and the other laser as a repump to return the atoms to the cooling transition if they end in the other hyperfine state  $m_f = 7/2$ . In our setup, as shown in Figure (16), we used one laser as a reference laser (DBR laser *PH770DBR080T8* from *Photodigm* and a current and temperature controller of *LDC 501* from *Stanford Research System*). The reference laser is locked on the  $|F = 2\rangle \rightarrow |F' = 3\rangle$  on the  $D_2$  transition in  $^{39}\text{K}$ . The reference laser is locked to room temperature on the vapor cell with  $^{39}\text{K}$  atoms; hence, we need to use Saturated Absorption Spectroscopy (SAS) (4). The two other lasers are locked with Offset locking [44] to the reference laser. That configuration was used because wide tunability range was needed for the lasers (we cannot obtain that by using ). Theoretically, the shift between the reference laser to the cooling laser, as described in Figure(I7), is

$$f_{\text{cooling}} = f_{\text{reference}} + 804.85 \text{ MHz}$$

An AOM was placed as a switch before the fiber with  $-100$  MHz shift, and determined a red detuning of  $3\Gamma \approx 18$  MHz. Therefore,

$$\Delta f_{\text{cooling}} = 922 \text{ MHz}$$

In addition, the theoretical shift between the reference laser to the cooling laser is

$$f_{\text{repump}} = f_{\text{reference}} - 431 \text{ MHz}$$

A AOM was placed as a switch before the fiber with  $+110$  MHz shift, and determined a red detuning of  $3\Gamma \approx 18$  MHz. Therefore,

$$\Delta f_{\text{cooling}} = 522 \text{ MHz}$$

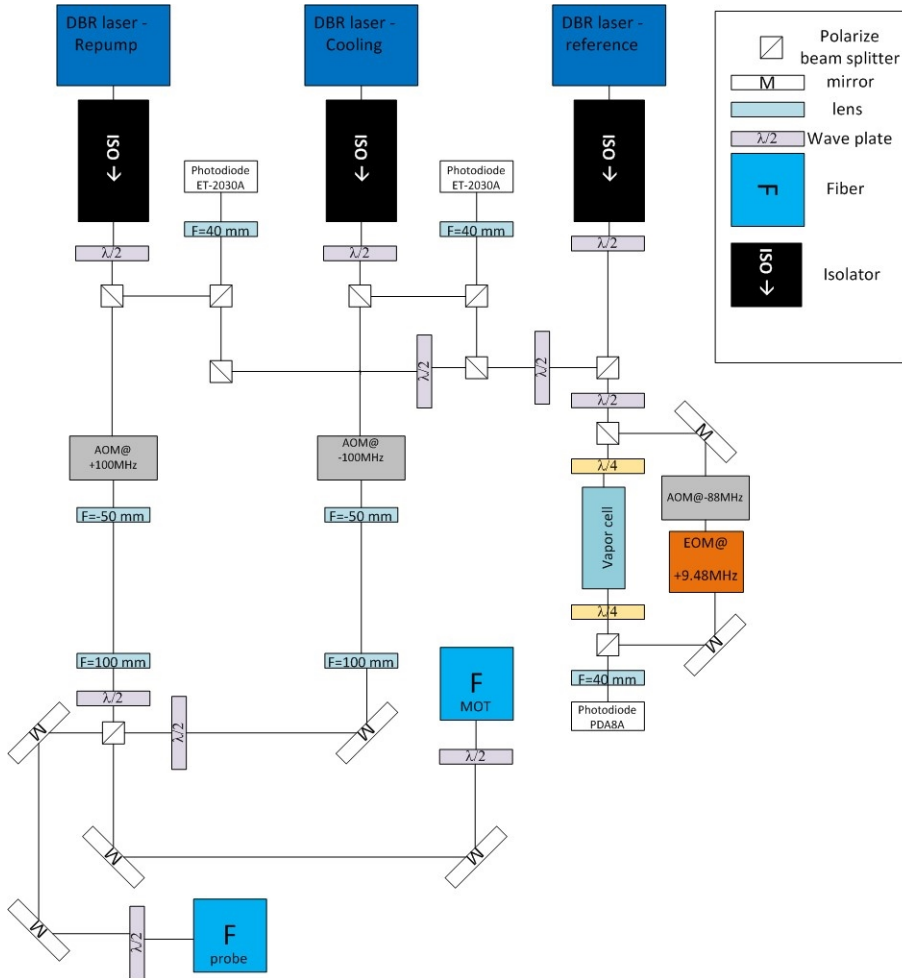


Figure 16: Laser setup. Cooling and repump are locked by offset locking to the reference laser. The reference laser locked on  $|F = 2\rangle \rightarrow |F' = 3\rangle$  in the  $D_2$  transition of  $^{39}\text{K}$  with SAS system. Most of the power of the lasers (cooling and repump) goes through a AOM that is used as a switch. After a 1:2 telescope, they are split, and the most injected to one fiber leads to the MOT, while the other power is injected to another fiber that lead to the probe.

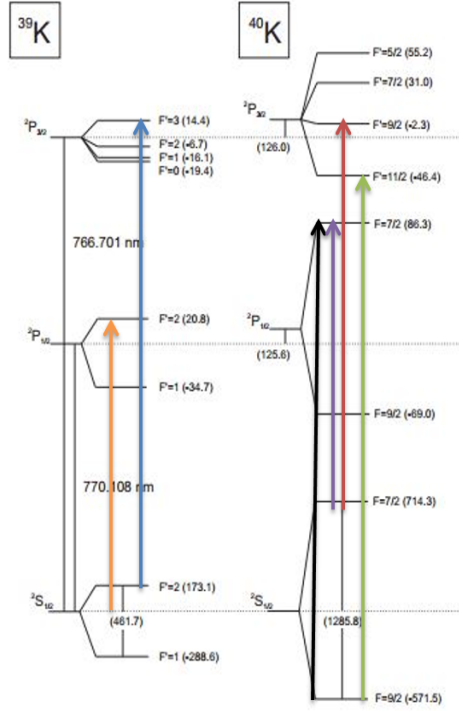


Figure 17: Optical transitions of the  $D_1$  and  $D_2$ -lines of  $^{39}\text{K}$  &  $^{40}\text{K}$ . The blue arrow is the transition that we lock to using the SAS for the MOT. The orange arrow is a transition used for the  $D_1$  cooling. The green arrow is the cooling transition, and the red arrow is the repump transition for the MOT. The black arrow is the cooling transition, and the purple arrow is the repump transition for the  $D_1$  cooling. The numbers are in MHz. Adopted from [28]

### 4.2.3 Saturated Absorption Spectroscopy (SAS)

In laser cooling, we must lock the laser to the frequency of an atomic transition. The atoms move with a random velocity distribution, so the laser comes into resonance with different velocity groups of atoms. Therefore, the laser interacts with atoms in different velocity groups of atoms. Their velocities, according to Maxwell-Boltzmann distribution, are

$$\frac{dn}{dv} = n_0 \sqrt{\frac{m}{2\pi k_B T}} \exp\left(\frac{-mv^2}{2k_B T}\right)$$




If the laser beam is at frequency  $f_0$  in the reference frame of the lab, than in the atoms frame, the frequency is shifted due to the Doppler effect:

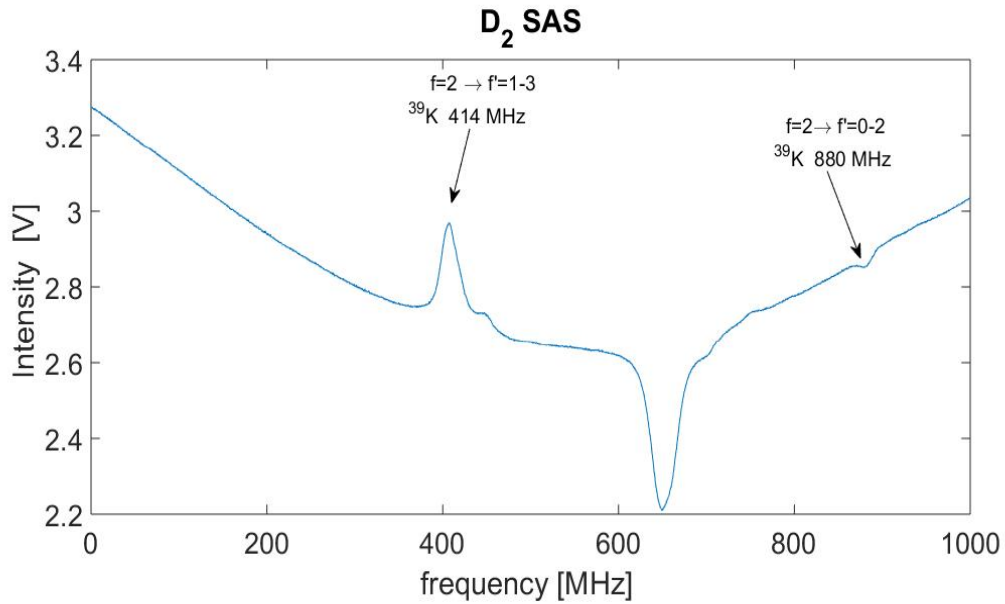
$$f = \left(1 \pm \frac{v}{c}\right) f_0$$

This means that each velocity group has a different resonance frequency in their respective frame of reference. Therefore, the intensity assumes Gaussian shape

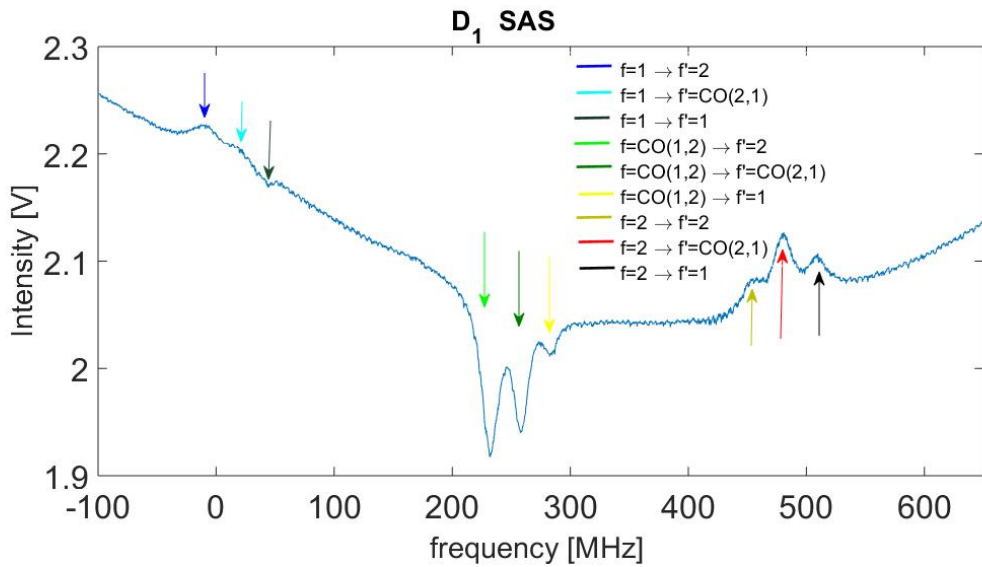
$$I(f) = I_0 \exp\left[-\frac{mc^2 (f_0 - f)^2}{2k_B T f^2}\right] \quad (17)$$

with a width of  $\sigma = f_0 \sqrt{\frac{k_B T}{mc^2}}$ . In  $^{39}K$  on temperature  $T \approx 340$  K, the intensity width  $\sigma = 346$  MHz. However, Doppler broadening makes it impossible to determine the precise transition frequency to within the natural linewidth ( $\Gamma \sim 6$  MHz). To overcome this difficulty, we need to use an SAS system that is a probe pump setup.


Two counter-propagating probe and pump, laser beams derived from a single laser beam are sent through an atomic vapor cell (in our lab, a vapor with  $^{39}K$ ) at room temperature with same frequency  $f_0$ . A photodiode is placed after the vapor cell and measured the probe beam. If the probe beam frequency is not at the resonance frequency,  $f_{\text{probe}} \neq f_0$ , then it interacts with atoms that have velocity  $v$  that satisfy the Doppler shift  $f_{\text{probe}} = f_0 (1 + v/c)$ . In addition, the pump beam interacts with atoms that have velocity  $-V$ . In this case, the signal on the photodiode is a deep  17) with width of  $\sigma$ . However, when the beam is on resonance  $f_{\text{probe}} = f_0$ , the atoms has zero velocity, and there is a sharp decrease in absorption (seen as a sharp increase in the signal from the detector), since many of these atoms have been pumped out of the ground state and are not be able to absorb any photons from the resonant probe beam. Figure 18a shows the signal from the SAS system with with  $^{39}K$  at room temperate for the  $D_2$  laser, and in Figure 18b shows another SAS system result for the  $D_1$  transition. The system description in Figure 16 for  $D_2$  and in Figure 25 for  $D_1$ .



(a)



(b)

Figure 18: Saturated Absorption Spectroscopy in our system.  Figure a) shows the  $D_2$  transition (figure17) where zero frequency is for the repump transition in  $^{40}K$ , and Figure b) shows the  $D_1$  transition (figure17), where zero frequency is the transition between  $F = 1 \rightarrow F' = CO(1,2)$  in  $^{39}K$ .

#### 4.2.4 Offset locking

Offset locking is a technique to lock a laser to the reference laser and give the ability of frequency tuning from tens of MHz to several GHz. This technique is based on the frequency depended phase shift experienced by the beat note of two laser frequencies, as shown in [44]. The circuit and the locking signal are shown in Figure 19.

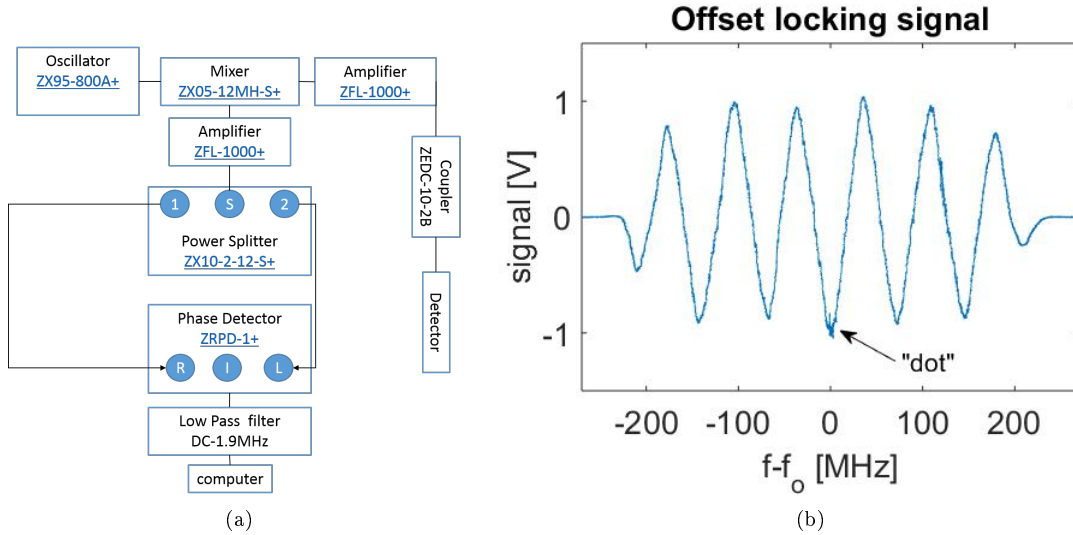



Figure 19: a) Offset Locking circuit. The signal is goes through a coupler (ZEDC-10-2B) to take a reference of  signal (and measure the laser width) and amplify (zfl-1000+). Then, it is mixed (zx-12MH-S+) with a voltage control oscillator (VCO-zx95-800A+). It then splits to two lines (ZX10-2-12-S+), one short and another long (0.1m & 3.4m). Afterwards, the two lines are recombined on a phase detector (ZRPD-1+). We use a low-pass filter of 1.9KHz at the end. b) offset signal. The “dot” position is controlled by the VCO

#### 4.2.5 Measurements of the number of atoms

To calculate the number of atoms, we measure their florescence with a photodiode. We can calculate the number of atoms by the following equation:

$$N = \frac{V\tau}{g_1 g_2 S \cdot E_{\text{photon}} \rho_6} \quad (18)$$

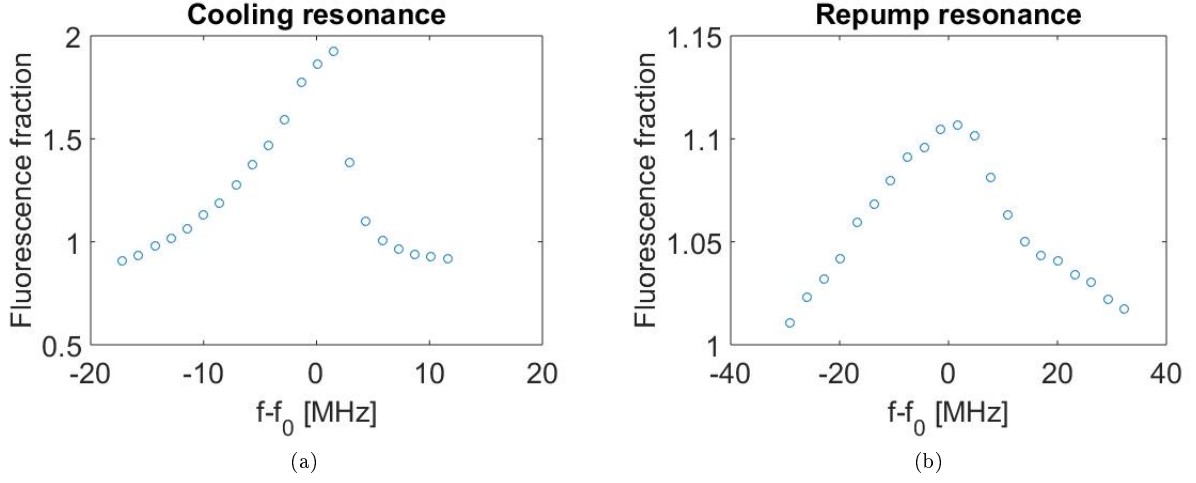


Figure 20: Calibration of the resonance frequencies. a) Cooling Laser Fluorescence Fraction. b) Repump Laser Fluorescence Fraction

where  $V$  is the measured output voltage,  $\tau$  is the excited state life time of the atom,  $g_1$  is the current to voltage photodiode gain,  $g_2$  is the photodiode efficiency,  $S$  is the solid angle fraction ( $S = \arctan\left(\frac{d}{f}\right)$ ),  $E_{\text{photon}}$  is the photon energy, and  $\rho_6$  is the excited state fraction that is calculated in [45] for a six-level model. To calibrate the laser detuning, we first find the resonance. We load the MOT for 15 sec with cooling laser frequency at  $f_0$  optimized for MOT operation, change in 10 msec the cooling laser frequency to  $f_1$ , and measure the fluorescence fraction  $\frac{V(f_1)}{V(f_0)}$ . By performing this sequence, we confirm that our signal does not depend on the number of atoms and  $f_0$ , but only on  $f_1$ . The result is shown in Figure (20a), and we repeat this measurement for the repump laser (Figure 20b). We optimized the lasers detuning (cooling and repump) to obtain a high number of atoms (see

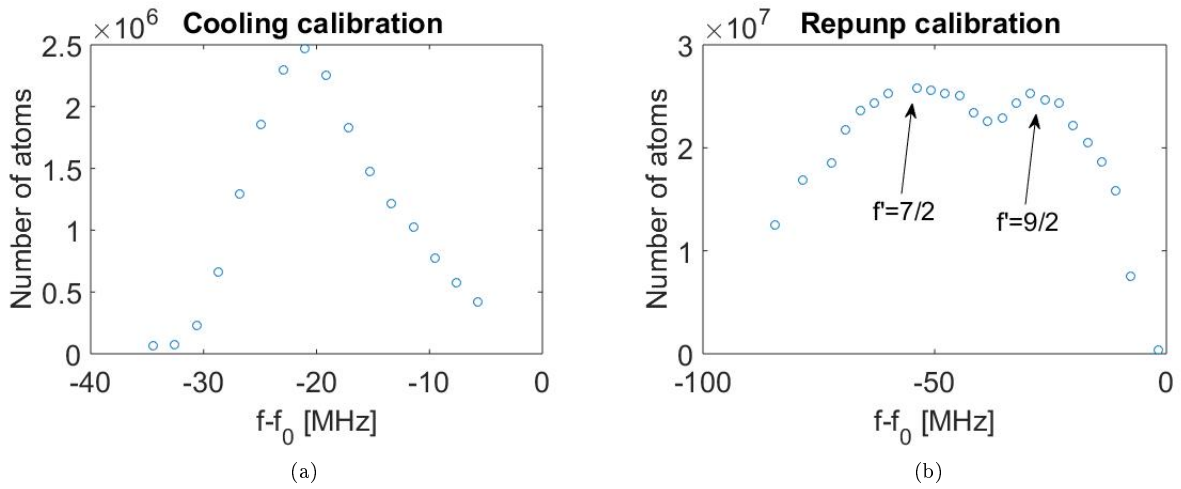


Figure 21: Number of atoms vs laser frequency. To know what are good conditions for the MOT, we scan the laser frequency and calculate the number of atoms. (a) Cooling Laser. (b) Repump Laser

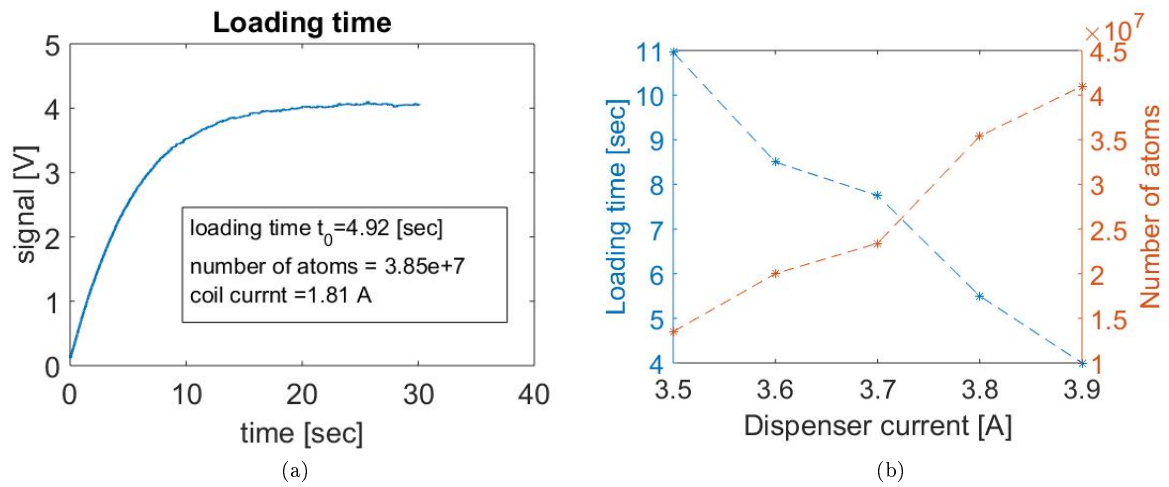


Figure 22: a) Example of loading time measurement. b) Number of atoms and loading time vs. dispenser current. High currents release more potassium-40 and increase the atoms density in the cell. Thus, the loading time decreases and the number of atoms increases. However, a high current shortens the life of the dispenser.













	$\delta t_1$	$\delta t_2$	$\delta t_3$	$\delta t_4$
MOT at $t_0$				
release				
recapture				

Figure 23: Release & Recapture Experiment. In a short time, most of the atoms do not escape from the area of the MOT beams so they are trapped again. However, as time progresses, the number of atoms that remain in the MOT beams decreases depending on their velocity or, in other words, their temperature.

Figure21a and Figure21b).

The last parameter that is tunable is the dispenser current. The dispenser current can shorten the loading time (Figure 22) and increase the number of atoms.

#### 4.2.6 Temperature Measurement with Release & Recapture Technique

To measure the MOT temperature, we use Release and Recapture (R & R) method [46] described in Figure (23). Assuming that the atoms in the MOT have a Maxwell Boltzmann distribution

$$f(v) = 4\pi v^2 \left( \frac{m}{2\pi k_B T} \right)^{3/2} e^{-\frac{mv^2}{2k_B T}}$$

At some point, we immediately shut off the trap and let the atoms expand ballistically for duration  $\delta t$  and then open the lasers again and recapture part of the atoms. The position of each atom after this expansion is given by

$$f(r, t) = \frac{4r^2}{\sqrt{\pi}\alpha^3 t^2} e^{-\frac{r^2}{\alpha^2 t^2}}$$

Where  $\alpha = \left( \frac{m}{2k_B T} \right)^{-3/2}$ . Now we can use  $v = r/t$  and obtain

$$f(v) = \frac{4v^2}{\sqrt{\pi}\alpha^3} e^{-\frac{v^2}{\alpha^2}}$$

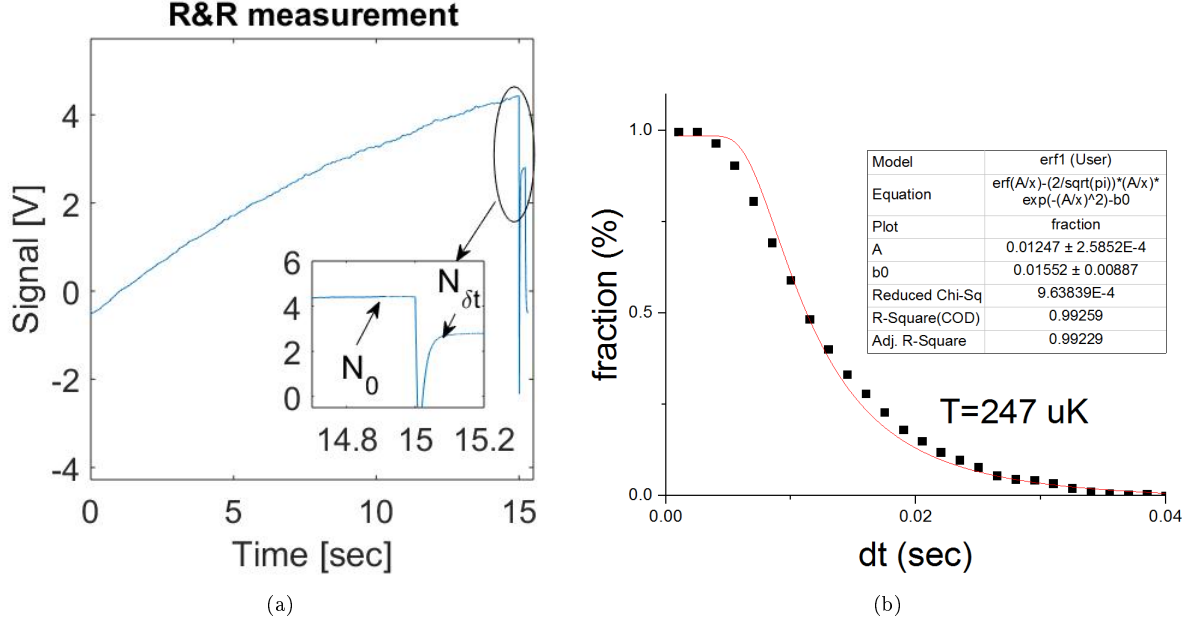


Figure 24: Release & Recapture Measurement. a) Example of sequence. We loaded the MOT and closed the lasers for  $\delta t$  and calculated the fraction of  $\frac{N_{\delta t}}{N_0}$ . b) Fraction vs.  $\delta t$ . From the fit, the temperature was calculated and showed  $T \approx 247 \mu\text{k}$ .

Assuming that the MOT radius starts with  $r_0$  and captures with the radius beam ( $r_f = \omega_0$ ), we can calculate the number of atoms that we trap

$$N(t) = \int_{r_0}^{r_f} N_0 f(v) dv = N_0 \frac{4}{\sqrt{\pi} \alpha^3 t^3} \int_0^{\omega_0} r^2 e^{-\frac{r^2}{\alpha^2 t^2}} dr$$

$$\Rightarrow \frac{N(t)}{N_0} = \text{erf}\left(\frac{\omega_0}{\alpha \cdot \delta t}\right) - \frac{2\omega_0 e^{-\frac{\omega_0^2}{\alpha^2 \delta t^2}}}{\alpha \cdot \delta t \sqrt{\pi}}$$

The fraction of the number of atoms in the MOT was measured after  $\delta t$  without lasers divided by the number of atoms before closing the trap (the results are shown in Figure(24)). We measured the MOT laser waist  $\omega_0 = 4.4 \text{ mm}$  and obtained  $\alpha = 0.01247 \pm 0.00258$ . Therefore, the temperature is

$T = 247 \pm 13 \mu\text{K}$ .

### 4.3 $D_1$ cooling

As explained in 3.1.3,  $D_1$  cooling can lower the temperature to  $T \approx 15 \mu\text{K}$  in  $^{40}\text{K}$  without atom loss. The following introduces our system and experimental results.

#### 4.3.1 Lasers setup

We used a DBR laser (*photodigm PH770DBR080T8*) at  $\lambda = 770.1 \text{ nm}$  and a current and temperature controller (*Stanford Research System LDC501*). We took a  $\sim 10 \text{ mW}$  towards an SAS system (4). We locked the laser with the derivative signal by a PID loop on the current of the laser.

The  $D_1$  cooling transition is  $|F = 9/2\rangle \rightarrow |F' = 7/2\rangle$ . However, we used a  $^{39}\text{K}$  for locking the laser and the most obvious line in locking signal is the crossover line  $|F = co(1,2)\rangle \rightarrow |F' = 2\rangle$ . 17 shows that to obtain the transition  $|F = 1\rangle \rightarrow |F' = 2\rangle$  we need to add  $230.85 \text{ MHz}$ . Now we need to move to the energy level of  $^{40}\text{K}$ . Therefore the cooling resonance is the following :

$$f_{\text{cooling}} = f_{\text{lock}} + 704.85 \text{ MHz}$$

We manage this with a three Acousto-Optic-Modulator (AOM). The first one is a double pass (*Gooch & Housego -AOM AOMO 3200-124*) configuration with  $230 \text{ MHz}$  on the  $-1$  order. This configuration gave the ability to change the frequency without changing the optic system (Outgoing angle does not change when changing the frequency of the AOM). The second AOM (*Gooch & Housego -AOM AOMO 3200-124*) has a frequency of  $200 \text{ MHz}$  ( $+1$  order).


The relation between the  $f_{\text{lock}}$  and  $f_{co(1,2)\rightarrow 2}$  is:

$$f_{\text{lock}} = f_{co(1,2)\rightarrow 2} - \frac{f_{\text{AOM-SAS}}}{2} - f_{\text{double-pass}}$$



Therefore, the frequency shift is

$$\begin{aligned}
 \Delta f &= f_{\text{cooling}(f=9/2 \rightarrow f'=7/2)} - f_{\text{lock}} \\
 &= 704.85 - 60 - 230 \times 2 \\
 &= 202.55 \text{ MHz}
 \end{aligned}$$

We added the third AOM ( *Gooch & Housego -AOM AOMO 3200-124*) at +200 MHz for the final frequency transition. Prior to the third AOM, we added a homemade Tapered Amplifier (TA) to increase the laser power. The beam after the TA diverges on an axis parallel to the optical table. Therefore, we added a cylindrical lens with  $f = 75$  mm. Afterward  added a telescope 4:1 to obtain a small beam for the third AOM. We took the first positive order and made another telescope 1:2 to match the beam mode to the fiber mode.

For the repump laser, we used the cooling beam and added a sideband by using home-made high frequency Electro-Optic-Modulator (EOM 4.3.2). Then, the laser beam is injected to three optical fibers (the 3D MOT fibers)

The power beam is controlled by changing the RF AOM power (with a voltage variable attenuator (*Mini circuits ZX73-2500-s+*)).

### 4.3.2 High Frequency Electro-Optic-Modulator

Cooling process requires two laser frequencies, one frequency for cooling and one frequency for repumping (3.1.2). In  $^{40}\text{K}$  the  $D_1$  transition has a distance of 1.285 GHz. Therefore, as in the MOT, we can take two different lasers locked by an offset locking technique. However, in  $D_1$  cooling, the frequency shift is the frequency shift between  $|-9/2\rangle \rightarrow |-7/2\rangle$  in  $^2S_{1/2}$ . In addition, in  $D_1$  cooling, the magnetic field is set to zero and the state distances are not changed. Therefore, we can use an Electro-Optic-Modulator (EOM) to add frequency side band on the top of the cooling laser that are  $\pm 1.285$  GHz apart from the main laser frequency.

EOMs are based on the linear Electro-Optic effect, which is the modification of the refractive index of a nonlinear crystal by electric field in proportion to the field strength. The electric field at  $\omega_0$  enters the medium that operates another electric field at  $\omega_m$ . Thus, the equation of the field is



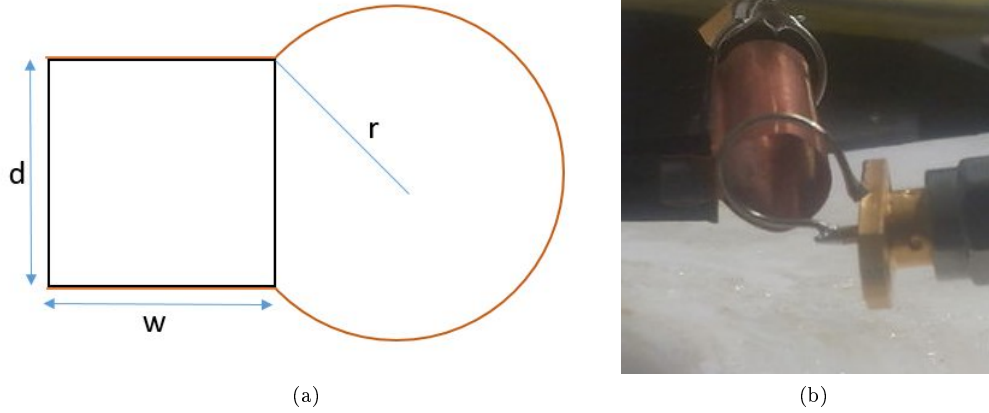


Figure 26: a) High Frequency EOM prescription. The black square with area of  $A = w * d$  is the crystal area cross section, and the brown with radius  $r$  is the foil with a thickness of  $0.1mm$ . b) EOM picture where one loop is for antenna and another is a pickup coil for Q factor measurement.

$$\begin{aligned}
 E(t) &= E_0 (\sin(\omega_0 t + n \sin(\omega_m t))) \\
 &= E_0 \sum_{n=0}^{\infty} J_n(n) \sin((\omega_0 + n\omega_m) t)
 \end{aligned}$$

This new phase can be applied by sending the electric field through a nonlinear crystal, resulting in a corresponding change in the refractive index. To make a significant change in the crystal, a high voltage needs to be produced with a frequency of  $\omega_m$  on the crystal. There are electronics that can generate a high frequency voltage of more than 1 GHz. Therefore, we needed to produce a resonant circuit [47]. A circuit from copper foil was constructed with a thickness of 0.1 mm and a loop with 3 mm space was made for contact with the crystal ( $LiNbO_3$ ) (Figure 26).

The crystal could be described as an ideal capacitor. Therefore,  $C = \epsilon w l / d$ , where  $\epsilon$  is a dielectric constant at  $\omega_m$ . Also the accumulative inductance of the copper foil loop can be described as an ideal cylinder current sheet (because  $2\pi r \gg d$ )  $L = \mu_0 \pi r^2 / l$ . Therefore, the resonant frequency of this  $CL$  circuit is given as

$$f_0 = \frac{1}{2\pi} \left( \frac{c}{r} \right) \left( \frac{d}{\pi w (\epsilon_w / \epsilon_0)} \right)^{1/2}$$

We used a crystal of dimensions  $w = d$ , and  $c$  is speed of light. For our experiment, ( $f_0 = 1.285$  GHz)  $r \approx 4.15$  mm (the value of  $\epsilon_w$  at this frequency is not known and we assume that it is  $\sim 43$ ).

In our lab, we used a  $LiNbO_3$  crystal with dimensions of  $3 \times 3 \times 30$  mm. If the crystal would have been smaller than 3 by 3 mm, then the gap would have been smaller, resulting in a larger electric field for a given power. However, the laser beam must travel through the crystal, and our laser beam is a 1.5 mm, Therefore, a crystal with dimensions of  $3 \times 3$  mm is well suited to our lab.

In addition, the design for this EOM was constructed as follows. The holder of the crystal is formed from Teflon to prevent unwanted changes to the resonator quality due to inductance.

Copper foil with a thickness of 0.1 mm was polished to maximize the transmission of the foil. Then, the foil was twisted on a drill with a diameter of 8.3 mm. Both sides of the copper cylinder were bent so a surface of 3 mm would fit the dimensions of the crystal.

A hole was made in the Teflon holder and threaded the RF antenna (end loop). For good coupling, the antenna was located as close to the copper foil cylinder as possible without blocking the path of the optical crystal or touching the foil. The antenna was connected to a VCO (*Mini Circuits ZX95-1410+*).

Next, the quality of the resonator was measured. The  $Q$  (quality) factor describes how much energy is lost in the resonator, with a large  $Q$  meaning less energy lost. The  $Q$  factor is defined as

$$Q = \frac{f_0}{\Delta f}$$

where  $\Delta f$  is the bandwidth (where the energy is reduced by half the maximum value) and  $f_0$  is the resonance frequency.

The  $Q$  factor was measured with an RF antenna and found that  $Q \approx 150$  and  $f_0 = 1.285$  GHz. This gave us the possibility of adjusting the device. The direction was made by a squeeze of the

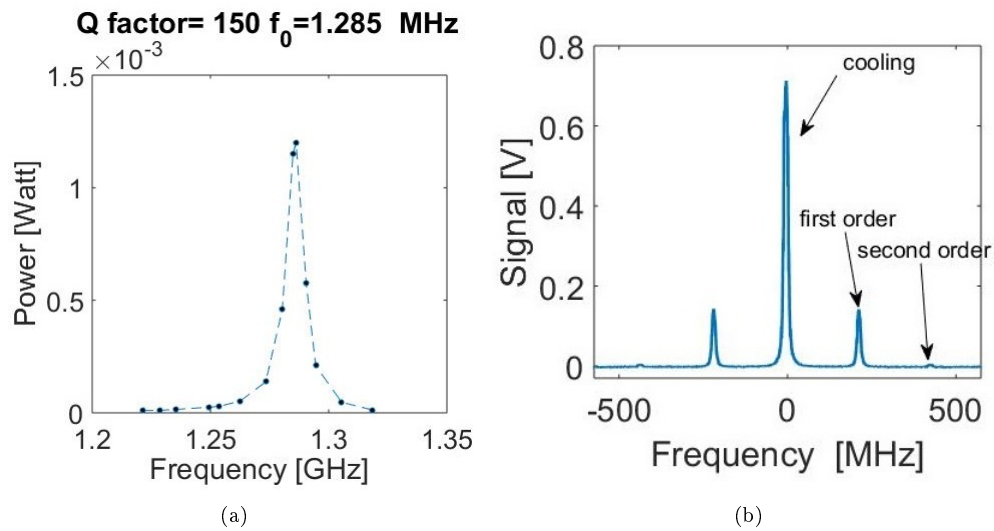


Figure 27: a) Measurement of Q factor  $Q \approx 150$  and  $f_0 = 1.285$  GHz. b) Measurement of EOM efficiency using Fabry Perot. The maximum efficiency (at high RF power  $\sim 4$ W) of the EOM is  $\frac{I_{\text{repump}}}{I_{\text{cooling}}} = 0.19$ . The Fabry Perot scanning is 1.5 GHz, and the first-order peak distance is  $1500 - 216 = 1284$  MHz (this figure shows the sideband from the next peak where the distance between them is 1.5 GHz).

resonator, reducing the radius and thus increasing the resonant frequency. In addition, we studied the effect on the laser by measuring the laser in a Fabry Perot. An RF power of  $P = 4$  W and obtain  $\frac{I_{\text{repump}}}{I_{\text{cooling}}} = 7.5\%$  (Figure 27b), which should be sufficient for the  $D_1$  cooling.

### 4.3.3 Measurement of the $D_1$ Frequency Resonance

In the first measurement, we wanted to find the resonance frequency of the cooling transition ( $|F = 9/2\rangle \rightarrow |F' = 7/2\rangle$ ). For this measurement, a Photo Multiplier Tube (PMT) measured the fluorescence of the atoms. We opened the PMT 3 ms before opening the  $D_1$  laser (just cooling), as the PMT has an opening time of  $\sim 2$  ms. When we opened the cooling laser, the atoms are fluorescent for  $\sim 100$   $\mu\text{s}$ . Therefore, the signal had an exponential decay. We made a fit of  $I = A_0 e^{-t/\tau}$  and took the  $A_0$  as the intensity of the atoms fluorescence while scanning over a range of  $f = 25$  MHz. We cannot scan over more than 25 MHz, as we scan on the double-pass AOM before the locking circuit, and any change in this AOM changes the intensity on the locking signal and the laser would lock out. We found that the cooling resonance is at  $f_{\text{AOM-DP}} = 221.175$  MHz with a width of 10.02 MHz. We set the cooling frequency with blue detuning at

$$f_{\text{DP-AOM}} = f_{\text{resonance}} + 3\Gamma = 233.675 \text{ MHz}$$

Next, we added the repump frequency to the cooling beam by using a High Frequency EOM. This laser has two frequencies that are injected to the three fiber of the 3D MOT (retro-reflection configuration). The power at each axis is approximately  $I = 12I_{\text{sat}}$  with  $\frac{I_r}{I_c} \sim 7.5\%$ . Before starting to reduce the temperature, the atoms must be compressed by adding a magnetic-trap for 2 ms (which causes increased temperature).

### 4.3.4 Temperature and atoms number measurement by Time Of Flight (TOF) technique

TOF measurements are performed by acquiring the absorption signal of the probe laser beam through the falling and expanding atomic cloud. There are several methods of measurement of temperature, R&R 4.2.6, MOT fluorescence spectrum analysis[48], forced-oscillation[49]. Another model

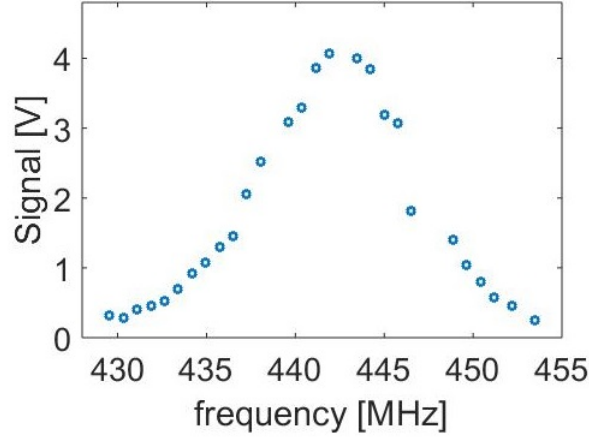


Figure 28: PMT signal Vs. DP-AOM frequency. The resonance is in  $2 \cdot f_{AOM-DP} = 443$  MHz. To cool with the blue detuning of  $\sim 3\Gamma$  on the  $D_1$  18 MHz was added. Therefore,  $2 \cdot f_{AOM-DP} = 461$  MHz. The final parameter is set by the parameters of the atoms (temperature and number of atoms) as shown in Figure 29.

that was suggested by Jerzy and Gawlik in [50] shows that the absorb signal from an atoms

$$N(t) = \frac{P_0}{2\pi(\sigma_I^2 + \sigma_t^2)} \exp \left[ - \left( \frac{g(t_0^2 - t^2)}{2\sqrt{2}\sqrt{\sigma_I^2 + \sigma_t^2}} \right)^2 \right]$$

where  $p_0$  is the probe laser power,  $t_0$  is the arrival time of atoms with no initial vertical velocity,  $\sigma_I$  are laser beam waist along  $x$  and  $y$  axes, and  $\sigma_t = \sqrt{\sigma_0^2 + \sigma_v^2 t^2}$  is the Gaussian radius of the ballistic expanded cloud. The Gaussian radius  $\sigma_v$  of the velocity distribution is associated with the temperature  $T$  of the atoms cloud by

$$T = \frac{m}{k_B} \sigma_v^2$$

After a loading time of 30 sec, we closed the coil current and the  $D_2$  laser beam and opened the  $D_1$  cooling for  $t = 4$  ms. We then closed the  $D_1$  laser, waited 18 ms, and then took a TOF image. The parameters of the cooling and repump frequency were scanned and these parameters were optimized as described in Figure 29. At the end, the atoms parameters were  $T = 19 \mu\text{K}$  and  $N = 2 \times 10^8$  atoms (where  $f_{AOM-DP} = 461.3$  MHz,  $f_{\text{repump}} = 1287$  MHz and  $D_1$  duration  $t = 4$  ms). The TOF image is

shown in Figure 29d.

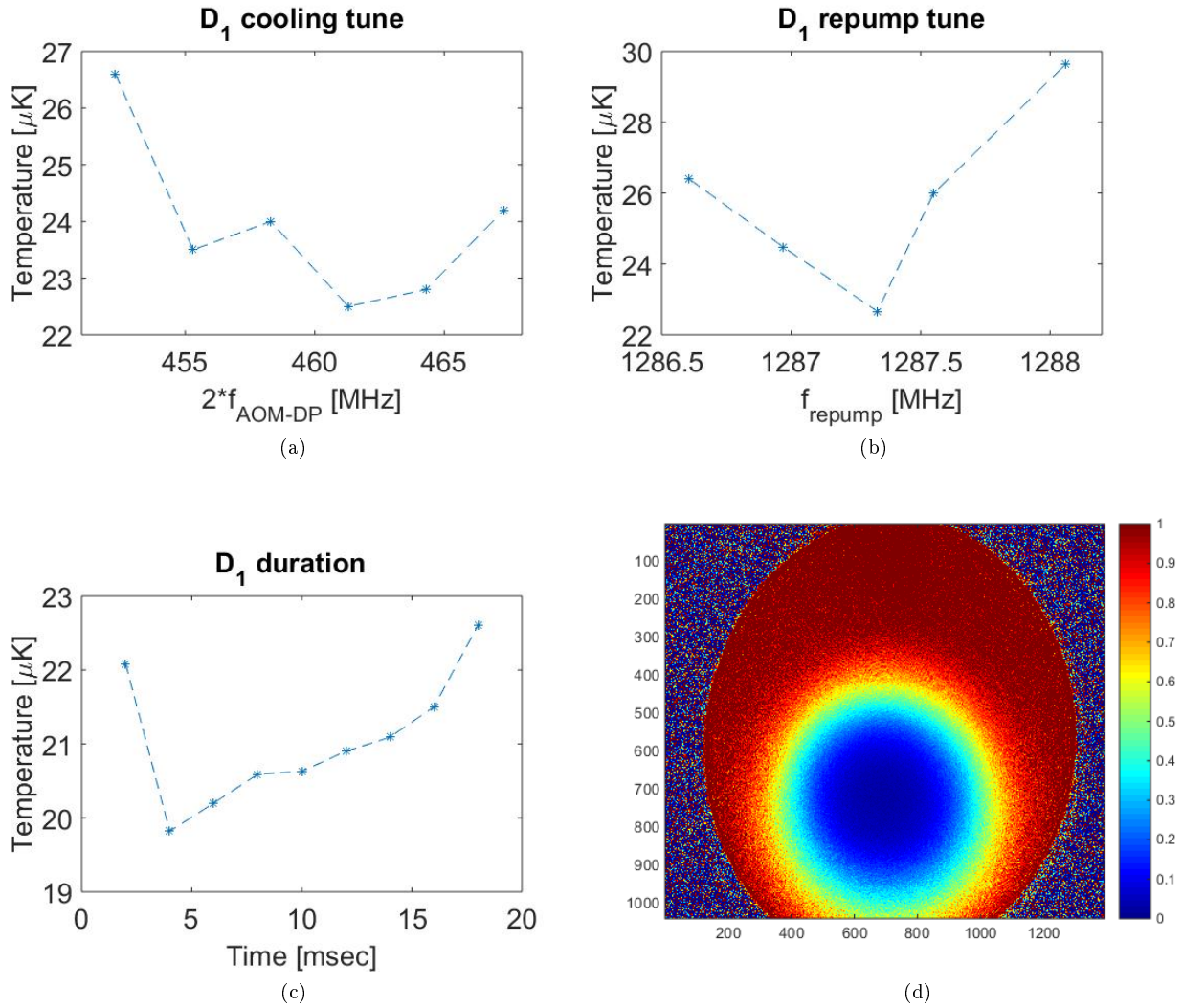


Figure 29: a)  $D_1$  cooling tune vs temperature. b)  $D_1$  repump tune vs temperature. c)  $D_1$  duration vs temperature d) Absorb image of atoms after  $D_1$  cooling with Time Of Flight  $t = 18$  ms.

#### 4.4 Optical Trap

As shown in equation (16), in a optical trap, the potential and the scattering rate depend on the beam  $\omega_0$



$$U_{\text{dip}} \propto \omega_0^{-5}$$

Therefore, we need precise measurement of the beam waist. In addition, a laser with  $\lambda = 1064 \text{ nm}$  should be used to obtain a long lifetime in the microtrap (2).

#### 4.4.1 Microtrap waist measurement

To know the optical trap's depth and size, we need to measure the  $\omega_0$  of the beam. Each camera has a finite size of the pixel that is greater than  $7 \text{ }\mu\text{m}$ , we can not use a camera to measure the waist. We can use a knife edge measurement, but again, we need a high resolution x-z stage ( $< 0.2 \text{ }\mu\text{m}$  for seven less measurements at the waist).

We used two easy ways to measure the micro-trap waist by using the Knife edge technique in a different way [51]. For Gaussian beam the one dimensional profile is given by

$$V = \frac{P_0}{2} \left( 1 \pm \text{erf} \left( \frac{\sqrt{2}(x - x_0)}{w_0} \right) \right)$$

where  $P_0$  is the laser power and  $\omega_0$  is the beam waist. In our setup, a collimated laser beam with waist  $\omega_1 = 0.89 \text{ mm}$  and  $\lambda = 1064 \text{ nm}$  enters a 1:6 telescope. It then travels through an Aspheric lens with  $f = 26 \text{ mm}$ . The Numerical Aperture (NA) is given by

$$NA = \frac{2 \cdot 6 \cdot \omega_1}{2f} = 0.205$$

The NA of a Gaussian laser beam is then reduced to its minimum spot size by

$$NA = \frac{\lambda}{\pi\omega_0}$$

where  $\lambda$  is the laser wavelength (in our trap,  $\lambda = 1064 \text{ nm}$ ) and  $\omega_0$  is the laser beam waist at the focus. Therefore,

$$\omega_{0,\text{theory}} = \frac{\lambda}{\pi \cdot NA} = 1.65 \text{ }\mu\text{m}$$

#### 4.4.2 Measurement of a microtrap waist with an optical chopper

An optical chopper is a spinning wheel with holes at a constant frequency. The holes are used as a knife for the knife edge measurement. A photodiode was placed after the chopper and measured power vs. time on a digital scope. By knowing the frequency of the chopper and the distance between the laser and the center of the chopper, we can calculate the velocity of the knife. Therefore, we can translate the time to distance.

#### 4.4.3 Measurement of the microtrap waist with a piezoelectric actuator and Michelson interferometer

In this measurement, a Piezoelectric actuator (*Thorlabs AE0203D08F*) was inserted to a translation stage. In our lab, we only have an actuator that can travel at  $9.1 \mu\text{m}$ . The actuator receives a voltage of  $0 - 150$  Volt from a ramp waveform. On the translation stage, a knife was set and measured the power on the photodiode. We can assume that the actuator travels linearly from  $0 \rightarrow 9.1 \mu\text{m}$ , but we can calibrate this with a Michelson interferometer (calculate the actuator traveling distance). As described in Figure (30a), our collimated laser beam  $\lambda = 1064 \text{ nm}$  was split with a Non Polarizing Beam Splitter (NPBS) to two mirrors. One mirror is moved with the translation stage by the actuator, and the second mirror does not move. The lasers from the two mirrors are combined on the NPBS and focused on a photodiode. On the photodiode, we obtain a diffraction pattern that is dependent on the difference between the optical paths [52].

$$\Delta L = \frac{\lambda m}{2}$$

where  $\Delta L$  is the distance that the mirror is moved,  $m$  is the number of maximums, and  $\lambda$  is the wavelength of the laser. As shown in Figure 30b, we obtain  $m = 14.5$  in one waveform period; therefore,

$$\Delta L = 7.714 \mu\text{m}$$

Now, the distance in the knife edge measurement was measured as  $\omega_0 = 2.148 \mu\text{m}$  (figure 31). However, these measurements do not provide information regarding aberration or about  $M^2$ . To measure them,

there measurements of  $\omega(z)$  are needed, but for this, a long-travel Piezoelectric actuator is needed ( $\Delta L > 15 \cdot \omega_0$ ).

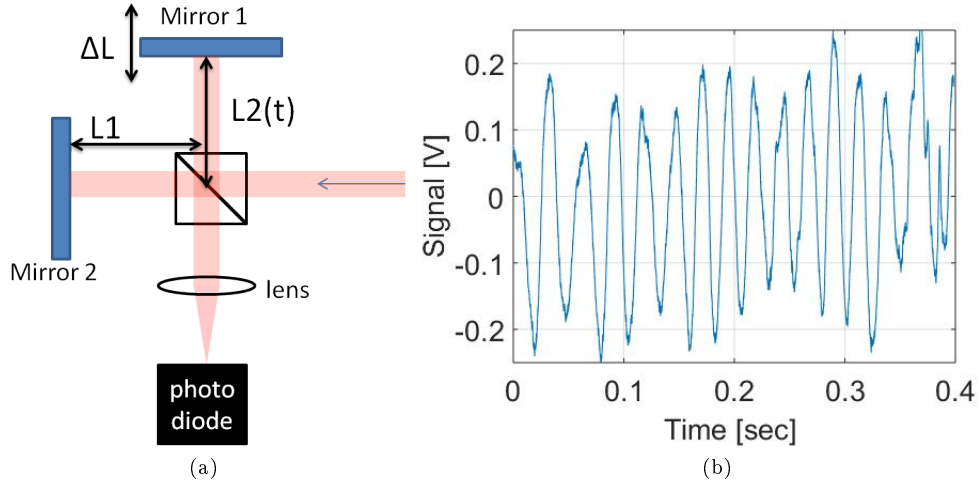


Figure 30: Measuring the Microtrap Waist with a Piezoelectric Actuator and a Michelson Interferometer. a) The system description. Collimated laser beam split by NPBS and traveling to two mirror (mirror 1 is on the translation stage and mirror 2 is fixed). They reflected back and combined on the NPBS and focused on a photodiode. b) Interferometer result. The figure shows that we obtain 14.5 maximum peaks, so the actuator travel is  $7.714 \mu\text{m}$  and, that the travel path of the piezo actuator is not linear (the frequency of the sin function is not the same).

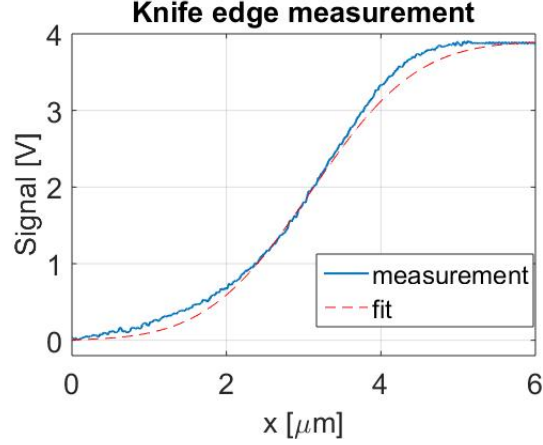


Figure 31: Calculation of the beam waist with Knife edge technique.

## 5 Summery and Future Plan

This study presents our new platform for quantum computation. It is based on fermion statistics and the attributes of ultracold atoms. Chapter 1 introduces the fundamentals of quantum computing and the features of ultracold atom.

Chapter 2 demonstrates the theory behind quantum computation solutions for our system. In addition, the explained one-qubit gates and two-qubit gates in ultracold fermion systems are presented. Moreover, the chapter presented our indecision regarding the choice of system from between the **De-generate fermi gas system** (cooling to low temperature and then loading to a micro trap) or the **fast approach System** (loading to an optical microtrap and then cooling the atoms to ground state).

Chapter 3 presents the relevant background for ultracold atoms, and Chapter 4 describes our two systems that are in the middle of construction. Additionally, it shows the MOT trapping and cooling stage and  $D_1$  cooling with one laser.

For future research, we need to perform a more theoretical study on the system parameters, such as the velocity  $d(t)$  of one qubit without change the qubit state , defining  $U$  and  $t$  for a  $\sqrt{SWAP}$  gate to obtain fidelity  $\mathcal{F} = 1$ , and more.

From an experimental perspective, we need to reach several goals.

- Loading several atoms to a microtrap and developing the ability to measure a single atom.
- Reducing the number of atoms to one.
- Construction of two tunable microtraps with the application of one and two qubit gates.
- Numerical calculation of the gates parameter (e.g.,  $U$ ,  $t$ ,  $d(t)$ , trap parameter).

I hope that in a few years we will be able to provide answers to these and other issues.

## References

- [1] R. P. Feynman, “Simulating physics with computers,” *International journal of theoretical physics*, vol. 21, no. 6, pp. 467–488, 1982.
- [2] P. W. Shor, “Algorithms for quantum computation: Discrete logarithms and factoring,” in *Foundations of Computer Science, 1994 Proceedings., 35th Annual Symposium on*, pp. 124–134, IEEE, 1994.
- [3] L. K. Grover, “Quantum mechanics helps in searching for a needle in a haystack,” *Physical review letters*, vol. 79, no. 2, p. 325, 1997.
- [4] J. I. Cirac and P. Zoller, “Quantum computations with cold trapped ions,” *Physical review letters*, vol. 74, no. 20, p. 4091, 1995.
- [5] J. P. Home, D. Hanneke, J. D. Jost, J. M. Amini, D. Leibfried, and D. J. Wineland, “Complete methods set for scalable ion trap quantum information processing,” *Science*, vol. 325, no. 5945, pp. 1227–1230, 2009.
- [6] J. L. O’Brien, “Optical quantum computing,” *Science*, vol. 318, no. 5856, pp. 1567–1570, 2007.
- [7] C. Weitenberg, S. Kuhr, K. Mølmer, and J. F. Sherson, “Quantum computation architecture using optical tweezers,” *Physical Review A*, vol. 84, no. 3, p. 032322, 2011.
- [8] A. Imamog, D. D. Awschalom, G. Burkard, D. P. DiVincenzo, D. Loss, M. Sherwin, A. Small, *et al.*, “Quantum information processing using quantum dot spins and cavity qed,” *Physical Review Letters*, vol. 83, no. 20, p. 4204, 1999.
- [9] R. Barends, J. Kelly, A. Megrant, A. Veitia, D. Sank, E. Jeffrey, T. C. White, J. Mutus, A. G. Fowler, B. Campbell, *et al.*, “Superconducting quantum circuits at the surface code threshold for fault tolerance,” *Nature*, vol. 508, no. 7497, pp. 500–503, 2014.
- [10] D. P. DiVincenzo *et al.*, “The physical implementation of quantum computation,” *arXiv preprint quant-ph/0002077*, 2000.

- [11] D. Loss and D. P. DiVincenzo, “Quantum computation with quantum dots,” *Physical Review A*, vol. 57, no. 1, p. 120, 1998.
- [12] M. A. Nielsen and I. L. Chuang, *Quantum computation and Quantum information*. Cambridge University Press India, 2000.
- [13] J. Preskill, “Reliable quantum computers,” in *Proceedings of the Royal Society of London A: Mathematical, Physical and Engineering Sciences*, vol. 454, pp. 385–410, The Royal Society, 1998.
- [14] L. W. Cheuk, M. A. Nichols, M. Okan, T. Gersdorf, V. V. Ramasesh, W. S. Bakr, T. Lompe, and M. W. Zwierlein, “Quantum-gas microscope for fermionic atoms,” *Physical review letters*, vol. 114, no. 19, p. 193001, 2015.
- [15] G. Edge, R. Anderson, D. Jervis, D. McKay, R. Day, S. Trotzky, and J. Thywissen, “Imaging and addressing of individual fermionic atoms in an optical lattice,” *Physical Review A*, vol. 92, no. 6, p. 063406, 2015.
- [16] Y. H. Fung, P. Sompet, and M. F. Andersen, “Single atoms preparation using light-assisted collisions,” *Technologies*, vol. 4, no. 1, p. 4, 2016.
- [17] A. M. Kaufman, B. J. Lester, and C. A. Regal, “Cooling a single atom in an optical tweezer to its quantum ground state,” *Physical Review X*, vol. 2, no. 4, p. 041014, 2012.
- [18] F. Serwane, G. Zürn, T. Lompe, T. Ottenstein, A. Wenz, and S. Jochim, “Deterministic preparation of a tunable few-fermion system,” *Science*, vol. 332, no. 6027, pp. 336–338, 2011.
- [19] C. Chin, R. Grimm, P. Julienne, and E. Tiesinga, “Feshbach resonances in ultracold gases,” *Reviews of Modern Physics*, vol. 82, no. 2, p. 1225, 2010.
- [20] C. Regal and D. Jin, “Experimental realization of bcs-bec crossover physics with a fermi gas of atoms,” *arXiv preprint cond-mat/0601054*, 2006.
- [21] D. Harber, H. Lewandowski, J. McGuirk, and E. A. Cornell, “Effect of cold collisions on spin coherence and resonance shifts in a magnetically trapped ultracold gas,” *Physical Review A*, vol. 66, no. 5, p. 053616, 2002.

- [22] M.-O. Mewes, M. Andrews, D. Kurn, D. Durfee, C. Townsend, and W. Ketterle, “Output coupler for bose-einstein condensed atoms,” *Physical Review Letters*, vol. 78, no. 4, p. 582, 1997.
- [23] L. Allen and J. E. O. Resonance, “Two-level atoms dover publications inc,” *New York*, 1987.
- [24] S. Kuhr *et al.*, *A controlled quantum system of individual neutral atoms*. PhD thesis, Universitäts- und Landesbibliothek Bonn, 2003.
- [25] D. Hayes, P. S. Julienne, and I. H. Deutsch, “Quantum logic via the exchange blockade in ultracold collisions,” *Physical review letters*, vol. 98, no. 7, p. 070501, 2007.
- [26] J. Hubbard, “Electron correlations in narrow energy bands,” in *Proceedings of the Royal Society of London A: Mathematical, Physical and Engineering Sciences*, vol. 276, pp. 238–257, The Royal Society, 1963.
- [27] T. Esslinger, “Fermi-hubbard physics with atoms in an optical lattice,” *Annu. Rev. Condens. Matter Phys.*, vol. 1, no. 1, pp. 129–152, 2010.
- [28] T. Tiecke, “Properties of potassium,” *University of Amsterdam, The Netherlands, Thesis*, pp. 12–14, 2010.
- [29] C. Monroe, D. Meekhof, B. King, S. Jefferts, W. Itano, D. Wineland, and P. Gould, “Resolved-sideband raman cooling of a bound atom to the 3d zero-point energy,” *Physical Review Letters*, vol. 75, no. 22, p. 4011, 1995.
- [30] B. J. Lester, N. Luick, A. M. Kaufman, C. M. Reynolds, and C. A. Regal, “Rapid production of uniformly filled arrays of neutral atoms,” *Physical review letters*, vol. 115, no. 7, p. 073003, 2015.
- [31] R. Grimm, M. Weidemüller, and Y. B. Ovchinnikov, “Optical dipole traps for neutral atoms,” *Advances in atomic, molecular, and optical physics*, vol. 42, pp. 95–170, 2000.
- [32] H. R. Lewis Jr and W. Riesenfeld, “An exact quantum theory of the time-dependent harmonic oscillator and of a charged particle in a time-dependent electromagnetic field,” *Journal of Mathematical Physics*, vol. 10, no. 8, pp. 1458–1473, 1969.



- [33] D. J. Wineland, R. E. Drullinger, and F. L. Walls, “Radiation-pressure cooling of bound resonant absorbers,” *Physical Review Letters*, vol. 40, no. 25, p. 1639, 1978.
- [34] J. Dalibard and C. Cohen-Tannoudji, “Laser cooling below the doppler limit by polarization gradients: simple theoretical models,” *JOSA B*, vol. 6, no. 11, pp. 2023–2045, 1989.
- [35] M. Landini, S. Roy, L. Carcagní, D. Trypogeorgos, M. Fattori, M. Inguscio, and G. Modugno, “Sub-doppler laser cooling of potassium atoms,” *Physical Review A*, vol. 84, no. 4, p. 043432, 2011.
- [36] G. Modugno, C. Benkő, P. Hannaford, G. Roati, and M. Inguscio, “Sub-doppler laser cooling of fermionic 40 k atoms,” *Physical Review A*, vol. 60, no. 5, p. R3373, 1999.
- [37] D. R. Fernandes, F. Sievers, N. Kretzschmar, S. Wu, C. Salomon, and F. Chevy, “Sub-doppler laser cooling of fermionic 40k atoms in three-dimensional gray optical molasses,” *EPL (Europhysics Letters)*, vol. 100, no. 6, p. 63001, 2012.
- [38] H. J. Metcalf and P. van der Straten, “Laser cooling and trapping of atoms,” *JOSA B*, vol. 20, no. 5, pp. 887–908, 2003.
- [39] V. Letokhov, V. Minogin, and B. Pavlik, “Cooling and capture of atoms and molecules by a resonant light field,” *Soviet Journal of Experimental and Theoretical Physics*, vol. 45, p. 698, 1977.
- [40] E. Arimondo and G. Orriols, “Nonabsorbing atomic coherences by coherent two-photon transitions in a three-level optical pumping,” *Lettere Al Nuovo Cimento (1971-1985)*, vol. 17, no. 10, pp. 333–338, 1976.
- [41] J. A. Christensen and R. F. Squires, “4-phenylpiperidine compounds,” Feb. 8 1977. US Patent 4,007,196.
- [42] T. Esslinger, I. Bloch, and T. W. Hänsch, “Bose-einstein condensation in a quadrupole-ioffe-configuration trap,” *Physical Review A*, vol. 58, no. 4, p. R2664, 1998.
- [43] K. Dieckmann, R. Spreeuw, M. Weidemüller, and J. Walraven, “Two-dimensional magneto-optical trap as a source of slow atoms,” *Physical Review A*, vol. 58, no. 5, p. 3891, 1998.

- [44] U. Schünemann, H. Engler, R. Grimm, M. Weidemüller, and M. Zielonkowski, “Simple scheme for tunable frequency offset locking of two lasers,” *Review of Scientific Instruments*, vol. 70, no. 1, pp. 242–243, 1999.
- [45] R. S. Williamson III, *Magneto-optical trapping of potassium isotopes*. PhD thesis, UNIVERSITY OF WISCONSIN–MADISON, 1997.
- [46] D. S. Weiss, E. Riis, Y. Shevy, P. J. Ungar, and S. Chu, “Optical molasses and multilevel atoms: experiment,” *JOSA B*, vol. 6, no. 11, pp. 2072–2083, 1989.
- [47] J. Kelly and A. Gallagher, “Efficient electro-optic modulator for optical pumping of na beams,” *Review of scientific instruments*, vol. 58, no. 4, pp. 563–566, 1987.
- [48] C. Westbrook, R. Watts, C. Tanner, S. Rolston, W. Phillips, P. Lett, and P. Gould, “Localization of atoms in a three-dimensional standing wave,” *Physical review letters*, vol. 65, no. 1, p. 33, 1990.
- [49] P. Kohns, P. Buch, W. Süptitz, C. Csambal, and W. Ertmer, “On-line measurement of sub-doppler temperatures in a rb magneto-optical trap-by-trap centre oscillations,” *EPL (Europhysics Letters)*, vol. 22, no. 7, p. 517, 1993.
- [50] T. M. Brzozowski, M. Maczynska, M. Zawada, J. Zachorowski, and W. Gawlik, “Time-of-flight measurement of the temperature of cold atoms for short trap-probe beam distances,” *Journal of Optics B: Quantum and Semiclassical Optics*, vol. 4, no. 1, p. 62, 2002.
- [51] J. M. Khosroffian and B. A. Garetz, “Measurement of a gaussian laser beam diameter through the direct inversion of knife-edge data,” *Applied Optics*, vol. 22, no. 21, pp. 3406–3410, 1983.
- [52] P. Fox, R. Scholten, M. Walkiewicz, and R. Drullinger, “A reliable, compact, and low-cost michelson wavemeter for laser wavelength measurement,” *American Journal of physics*, vol. 67, no. 7, pp. 624–630, 1999.